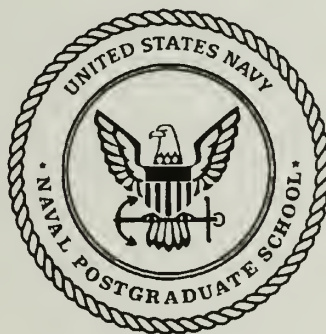


NAVAL POSTGRADUATE SCHOOL

Monterey, California



**COASTAL ACOUSTIC TOMOGRAPHY DATA
CONSTRAINTS APPLIED TO A
COASTAL OCEAN CIRCULATION MODEL**

by

Le Ngoc Ly
Ching-Sang Chiu

Final Report for Period June 1993-March 1994

April 1994

Approved for public release; distribution is unlimited

Prepared for: Office of Naval Research
Arlington, VA 22217-5000

72d Doc
D-02.14/2 NPS-02-72-001

NAVAL POSTGRADUATE SCHOOL
MONTEREY, CA 93943

Rear Admiral Thomas A. Mercer
Superintendent

Harrison Shull
Provost

This report was prepared for and funded by the Office of Naval Research, Arlington, VA 2217-5000.

Reproduction of all or part of this report is authorized.

This report was prepared by:

REPORT DOCUMENTATION PAGE

Form Approved
OMB No. 0704-0188

Public reporting burden for this collection of information is estimated to average 1 hour per response, including the time for reviewing instructions, searching existing data sources, gathering and maintaining the data needed, and completing and reviewing the collection of information. Send comments regarding this burden estimate or any other aspect of collection of information, including suggestions for reducing this burden, to Washington Headquarters Services, Directorate for Information Operations and Reports, 1215 Jefferson Davis Highway, Suite 1204, Arlington, VA 22202-4302, and to the Office of Management and Budget, Paperwork Reduction Project (0704-0188), Washington, DC 20503.

DUBLEY KNOX LIBRARY
NAVAL POSTGRADUATE SCHOOL
MONTEREY CA 93943-5101

1. AGENCY USE ONLY (Leave blank)		2. REPORT DATE April 1994		3. REPORT TYPE AND DATES COVERED Final Report (June 1993-March 1994)	
4. TITLE AND SUBTITLE Coastal Acoustic Tomography Data Constraints Applied to A Coastal Ocean Circulation Model				5. FUNDING NUMBERS	
6. AUTHOR(S) Le Ngoc Ly and Ching-Sang Chiu					
7. PERFORMING ORGANIZATION NAME(S) AND ADDRESS(ES) Naval Postgraduate School Dept of Oceanography Monterey, CA 93943-5000				8. PERFORMING ORGANIZATION REPORT NUMBER NPS-OC-94-001	
9. SPONSORING/MONITORING AGENCY NAME(S) AND ADDRESS(ES) Office of Naval Research Arlington, VA 22217-5000				10. SPONSORING/MONITORING AGENCY REPORT NUMBER N/A	
11. SUPPLEMENTARY NOTES The views expressed in this report are those of the authors and do not reflect the official policy or position of the Department of Defense or the U.S. Government					
12a. DISTRIBUTION/AVAILABILITY STATEMENT Approved for public release; distribution is unlimited				12b. DISTRIBUTION CODE A	
13. ABSTRACT (Maximum 200 words) (See pages 2 - 3)					
14. SUBJECT TERMS Data Assimilation, Coastal Ocean Modeling, Coastal Acoustic Tomography, Direct Insertion				15. NUMBER OF PAGES	
				16. PRICE CODE N/A	
17. SECURITY CLASSIFICATION OF REPORT Unclassified	18. SECURITY CLASSIFICATION OF THIS PAGE Unclassified	19. SECURITY CLASSIFICATION OF ABSTRACT Unclassified	20. LIMITATION OF ABSTRACT Unlimited		

TABLE OF CONTENTS

1.	INTRODUCTION	4
2.	COASTAL ACOUSTIC TOMOGRAPHY	9
2.1	A Hybrid Ray/Mode Inverse Method	
2.2	Ray Travel Time	9
2.1.2	Mode Travel Time	10
2.1.3	Optimal Inverse Solution	12
3.	COASTAL OCEAN CIRCULATION MODEL FOR THE GULF OF SIRTE .	15
3.1	The Model	15
3.2	Model Parameters and Initialization	18
3.3	Data Direct Insertion Technique	19
4.	NUMERICAL EXPERIMENTS AND DISCUSSIONS.	21
4.1	The "True Ocean" Experiment TR.	22
4.2	The No Data Assimilated Experiment EX_0	23
4.3	The NE-SW Assimilation Experiment EX_1	24
4.4	The NW-SE Assimilation Experiment EX_2	26
4.5	The Combined Slices Assimilation Experiment EX_3	28
5.	SUMMARY	32

6.	ACKNOWLEDGMENT	35
7.	REFERENCES	36

ACKNOWLEDGMENT

The authors would like to thank Mr. Robert Peloquin of the Navy Ocean Modeling and Prediction Program (NOMP) at the Office of Naval Research (ONR) for his support under Contract N0001493WR22028. Special thanks from LNL to Drs. Tal Ezer and George Mellor of Princeton University for their Gulf Stream model and help. LNL wishes to thank Dr. Phu Luong (NAVOCEANO) for his interaction which has benefited this work. The authors would like to thank Dr. Jim Miller, Mr. Chris Miller and Mr. Stefan Hudson of the Coastal Ocean Acoustic Center (COACT) for their help in MATLAB. The authors want to thank Ms. Millie Fidel (Office of Research) for her help in the final form of the report. Computations were performed on the NPS CRAY-YMP super-computer.

**COASTAL ACOUSTIC TOMOGRAPHY DATA
CONSTRAINTS APPLIED TO A COASTAL OCEAN
CIRCULATION MODEL**

Le Ngoc Ly

Ching-Sang Chiu

Coastal Ocean Acoustic Center

Naval Postgraduate School

Monterey, CA 93943-5100

Abstract

A direct insertion scheme for assimilating coastal acoustic tomographic (CAT) vertical temperature sections into a multilevel, coastal primitive equation model for the Gulf of Sirte (Lybia) is investigated using computer simulation experiments. Although the model was developed for the whole Mediterranean Sea (MED), only a model sub-domain covering the Gulf of Sirte was used in this study. The model has realistic coastlines and bottom topography, and a coastal-following, curvilinear, nearly orthogonal, horizontal coordinate system with a horizontal resolution of about 10 by 10 *km*. The grid of the model was designed using a grid generation/focusing technique. The model has complete thermodynamics, second order turbulence closure, and 16 bottom-following (sigma) vertical levels. To generate the "true ocean" for this study, the model was first spun up for 30 days with the Levitus temperature and salinity and ECMWF wind climatologies, and then run for one year and more. The last 60 days of this control run were taken to represent "actuality."

A series of assimilation experiments was carried out in which CAT temperature slices synthesized from different CAT configurations based on the "true ocean" were inserted into the model at various time steps to examine the convergence of this direct insertion scheme. In all the assimilation experiments, after a spinup for 30 days, the model was then integrated with CAT slices inserted daily to produce "nowcast fields" for periods of 30 and 60 days.

Our results strongly indicate that the coastal model and the direct insertion scheme for CAT slices work well together. As time pro-

gresses, the CAT slices spread information out in nearly all directions in the Gulf of Sirte. The inserted data act as an initial convergence maker which forces the model to "lose" memory of the initial state and gradually converge to the "true ocean". The global rms error of the nowcast temperature fields in the sub- domain considered in an experiment involving five CAT sections decreases by about 50% after 30 days and 66% after 60 days of data assimilation. The rms errors of two other experiments involving only a single slice are reduced by 33% after 30 days. In all three experiments, the rate of convergence, as measured by the rms error, is approximately constant. It is expected that the convergence to the "true ocean" will be quicker with more frequent insertions and with more CAT sections.

It is seen from these experiments that the temperature information spreads out faster over the shallow-water areas. This may be due to stronger mixing, horizontal shear and interaction with topography resulting in an increase of horizontal diffusion. The temperatures at the mixed-layer level converge more rapidly to the "true temperatures" in comparison to the surface-level temperatures. All the CAT slices have almost the same effectiveness in improving the nowcast fields regardless of their horizontal orientations. Our experiments also show that convergence is not linearly proportional to the number of CAT slices assimilated. Our simulation results confirm that the internal forcing provided by vertical slices derived by CAT is not localized in physical space. They induce immediate correlation between the fully nonlinear primitive equation model and the "true ocean".

1 INTRODUCTION

In the past ocean modeling tended to proceed separately from observations, mainly due to the lack of synoptic observations to properly constrain the model physics. Two new technologies in today's Oceanography brings new large synoptic datasets. Satellites provide global maps of sea surface height (SSH), sea surface temperature (SST) and wind stress. The latter field is the most important surface forcing of the ocean circulation. The satellites give information on the physical characteristics of the ocean surface and the near-surface layer. On the other hand, Ocean acoustic tomography can provide quality 4-D data measuring the interior ocean structure. This underwater acoustic inverse technique uses travel time changes of sound pulses to map sound speed/temperature perturbation along various paths. The satellites and ocean tomography are highly complimentary ocean observing systems. The ability to efficiently assimilate these datasets into ocean models is key to ocean nowcasting and forecasting.

Ocean tomography has traditionally been used in deep water for mapping the "ocean weather." The adaptation of this technique from deep to shallow water poses many scientific and engineering challenges. New sensor systems, advanced sound propagation models, and optimal signal processing and mapping techniques that will work in complex coastal environments must be developed and tested at sea. Research into and development of coastal tomography is the main thrust of a collaboration between scientists and engineers at the Naval Postgraduate School (NPS) and Woods Hole Oceanographic Institution (WHOI). In August 1992, a first-generation coastal acoustic to-

mography (CAT) system was tested in the Barents Sea (Chiu et al., 1993, and Miller et al., 1993). This system consists of an electronically controlled sound source and a telemetered vertical hydrophone array (Von Der Heydt et al., 1992). Using such system, the two groups demonstrated that CAT is practical and can produce vertical slices of the coastal ocean temperature and sound speed fields at high temporal and spatial resolutions. An assessment of the potential performance of a coastal nowcasting system which assimilates CAT vertical slices into a state-of-the-art coastal ocean model is the focal point of a computer simulation study reported here.

In the assimilation of oceanographic datasets, numerical ocean models play a critical role in the advection and propagation of the information contained in the data. Two outstanding questions were raised by Ghil and Malanotte-Rizzoli (1991): (1) Can information provided only at the sea surface be transferred dynamically into the deep oceanic layers, thus reconstructing the deep circulation? (2) Can information provided only locally, in limited oceanic regions, be transferred to ocean areas far away from the data-dense region and which time and space scales are better estimated through the assimilation of local data? These issues, particularly pertaining to deep-ocean circulations, have been addressed by Ghil and Malanotte-Rizzoli (1991) as well as other experts working in the subject area. We will give a brief review of some of these previous computer simulation works which are somewhat related to our present work in studying the direct insertion approach and advection information process. The central difference between this work and the previous works is that this work focuses on nowcasting in the coastal oceans using CAT and a state-of-the-art coastal ocean model.

The problem of propagation of surface information to the ocean interior was first studied by Hurlburt (1986) and Thompson (1986). They both inserted the altimeter data directly at every grid points into a two-layer primitive equation models for the Gulf of Mexico. Focusing on the dynamic transfer of information from the surface to the deep layer, Hurlburt (1986) demonstrated the success of the numerical ocean model used in the reconstruction of deep circulation. Hurlburt showed that approximately two updates per eddy cycle (57 days) are required for the assimilation to be successful and provide convergence to the reference ocean and the convergence is clearly accelerated further when updating every 20 days. Thompson (1986) focused on the geoid error as it affects the assimilation of altimeter data for mesoscale ocean prediction. He showed that errors in the geoid on spatial scales comparable to the model grid resolution did not seriously degrade the forecast, even in dynamically active regions with large gradients in the geoid height where instability process has been observed to occur. Kindle (1986) used a one-layer reduced-gravity primitive equation model of the Gulf of Mexico to examine the methodology of incorporating satellite altimeter data into ocean forecasting model. His main result was that for a stationary circular eddy, approximately two track (either ascending or descending) across the eddy are sufficient to ensure adequate spatial resolution and an irregularly shaped eddy may require three or four tracks.

In a two-part study, Malanotte-Rizzoli and Holland (1986 and 1988; hereafter MRH) examined the transfer of information by advection from data localized in space to other regions of the ocean using an idealized, mid-latitude, multilayer, quasi-geostrophic (QG), eddy-resolving model and a direct inser-

tion technique, weighting observations by their distance from the grid point being updated. In the first part (MRH, 1986) they used a quasi-linear, steady state model ocean and the assimilated data were density measured along various hydrographic sections. The main result of the study is that a local section can be quite effective in determining flow in regions far away from the data section if the flow is simple, steady, and quasi-linear. The most effective data sections are meridional, long and far away from the ocean's western boundary. In the second part (MRH, 1988), they used a time-dependent, fully eddy-resolving model ocean and the assimilated data were sections with different orientations. They found that, on the short time scale of mesoscale variability, all the data sections considered are equally ineffective. A single data section is quite effective in driving the model to the reference ocean if the data insertion process is carried out for time longer than the model equilibration time. A single section of assimilated data is completely ineffective in driving the model toward reality over time scales comparable with the mesoscale variability. Their result also show that the model climatological mean after ten years of data assimilation becomes extremely similar to the climatological mean of the reference ocean.

For this present study, we use a highly-nonlinear, primitive equation, eddy-resolving, coastal model for the Gulf of Sirte (the Gulf of Lybia). The model uses curvilinear coordinates with coastal-following and nearly-orthogonal grid. The model physics include fully active thermodynamics and a second order turbulence closure. This coastal model was developed by adapting the Princeton Ocean Model (POM) for the Gulf Stream (Mellor and Ezer, 1991) to the Mediterranean Sea (MED). Previously, Mellor and Ezer

(1991) used POM and an optimal-interpolation altimeter-data assimilation scheme to study the quality of the nowcast and forecast fields in the Gulf Stream region. Here, we use the model to study the potential of using CAT for coastal ocean nowcasting. Our assessment is focused on the simple direct insertion approach. An interesting question is that what configurations of CAT in a shallow water region such as the Gulf of Sirte (Gulf of Lybia), where both topographic and nonlinear effects are strong, are most effective, i.e., lead to a large and widespread improvement of the nowcast fields. Our emphasis here is on the understanding of horizontal propagation of the information obtained by CAT, the effect of data insertion intervals on the nowcast fields, and the convergence rate associated with the direct insertion scheme using this state-of-the-art curvilinear, multilevel primitive equation coastal ocean model for the Gulf of Sirte.

The report is organized as follows. In the next section, we give a description of coastal acoustic tomography (CAT) with a focus on the inversion of tomographic data to obtain vertical temperature slices. The coastal ocean circulation model for the Gulf of Sirte is described in Section 3. The model was first used to simulate the "true ocean" and, subsequently, it was used to produce nowcast temperature fields with the assimilation of synthetic CAT slices for various CAT configurations. The direct insertion technique is also discussed in Section 3. In Section 4, the numerical experiments and the results are discussed. Section 5 gives a summary of our findings.

2 COASTAL ACOUSTIC TOMOGRAPHY

In contrast to deep water propagation, the arrivals from the multipaths due to a pulse excitation in a shallow-water environment tend to overlap in time. It is therefore difficult to resolve them individually with omni-directional or almost omni-directional receivers which are typically used in deep water tomographic applications. Vertical line arrays and beamforming techniques can be used to overcome this difficulty. The observed perturbations of the beamformed individual ray/mode travel times constitute the database of the coastal tomographic inverse scheme developed by Chiu et al. (1993). Their scheme is discussed next in detail.

2.1 A Hybrid Ray/Mode Inverse Method

Establishing the mathematical relations between the observations and the unknown structure is the first step in the development of any inverse scheme. In our case, the observations are the changes in ray and mode travel times, δt_j^r and δt_n^m , and the unknown ocean variable is perturbation of sound speed, δc , i.e., the deviation from a reference sound speed field \bar{c} . The reference ocean is allowed to be range dependent in our formulation.

2.1.1 Ray Travel Time

The relation of the travel time of a pulse signal along a raypath, t_j^r , to the speed of sound c is well known. The relation is

$$t_j^r = \int_{\Gamma} \frac{1}{c(\vec{x})} ds \quad (1)$$

where $\vec{x} = (x, y, z)$ is the position vector and s is the arclength along the path trajectory Γ_j connecting a source and a receiver. Replacing c by $\bar{c} + \delta c$ and t_j^r by $\bar{t}_j^r + \delta t_j^r$ and assuming the change in travel time due to path perturbation is of 2nd order, we obtain, through linearization,

$$\delta t_j^r = \int_{\Gamma_j} \frac{-1}{\bar{c}^2(\vec{x})} \delta c(\vec{x}) ds \quad (2)$$

2.1.2 Mode Travel Time

The derivation of the relation between δt_n^m and δc is less straight forward. The uniformly valid, asymptotic coupled-mode solution of Desaubies et al. (1986) shall be our starting point. This solution was obtained by expanding both the magnitude and phase of the modal horizontal structure in a perturbation series in powers of a small parameter μ , where μ is the ratio of the wavelength to the characteristic horizontal scale of the oceanic variability. The horizontal phase of the n -th mode, to $O(\mu^2)$, is given as

$$\theta_n = \int_0^r \kappa_n(r, \omega) \left[1 - \frac{1}{2} \sum_m \frac{A_{mn}^2(r, \omega)}{\kappa_n^2(r, \omega) - \kappa_m^2(r, \omega)} \right] dr \quad (3)$$

where r is the range along the horizontal mode path connecting a source and a receiver, κ_n and κ_m are the horizontal wavenumbers of modes n and m , respectively, and A_{mn} is a coupling coefficient that can be equated as

$$A_{mn} = \int_0^\infty \frac{1}{\rho(r, z)} \left[Z_n(z; r, \omega) \frac{\partial Z_m(z; r, \omega)}{\partial r} - Z_m(z; r, \omega) \frac{\partial Z_n(z; r, \omega)}{\partial r} \right] dz \quad (4)$$

In the depth integral of (4), ρ is density, and Z_n and Z_m are the n th and m th modes, respectively.

Analogous to the "static ray approximation," we assume that the variations in the mode functions produce higher-order changes in the horizontal

phases comparing to those caused directly by the variations in the horizontal wavenumbers due to a perturbation in sound speed. This "static mode approximation" was introduced by Rajan et al. (1987) in their inverse method for obtaining geo parameters. Under this assumption, the variation of the modal phase integral (3) leads to

$$\delta\theta_n = \int_0^\infty (\delta\kappa_n + \sum_m f_{mn}\delta\kappa_n + \sum_m g_{mn}\delta\kappa_m)dr \quad (5)$$

with

$$f_{mn} = \frac{1}{2} \frac{(\bar{\kappa}_n^2 + \bar{\kappa}_m^2) \bar{A}_{mn}^2}{(\bar{\kappa}_n^2 - \bar{\kappa}_m^2)^2} \quad (6)$$

$$g_{mn} = -\frac{\bar{\kappa}_n \bar{\kappa}_m \bar{A}_{mn}^2}{(\bar{\kappa}_n^2 - \bar{\kappa}_m^2)^2} \quad (7)$$

where the modal quantities with an "overbar" are those associated with the reference ocean. From a stationary phase consideration, modal travel time and phase are related by

$$t_n^m = \frac{\partial\theta_n}{\partial\omega} \quad (8)$$

It follows from (8) and (5) that the variation in modal travel time is

$$\begin{aligned} \delta t_n^m &= \frac{\partial\delta\theta_n}{\partial\omega} \\ &= \int_0^r \left(\frac{\partial\delta\kappa_n}{\partial\omega} + \sum_m \frac{\partial f_{mn}}{\partial\omega} \delta\kappa_n + \sum_m f_{mn} \frac{\partial\delta\kappa_n}{\partial\omega} \right. \\ &\quad \left. + \sum_m \frac{\partial g_{mn}}{\partial\omega} \delta\kappa_m + \sum_m g_{mn} \frac{\partial\delta\kappa_m}{\partial\omega} \right) dr \end{aligned} \quad (9)$$

To find the relation between δt_n^m and δc , we need the relations of $\delta\kappa_n$ and hence $\frac{\partial\delta\kappa_n}{\partial\omega}$ to δc . Using the governing vertical-structure equation and

orthonormal condition for the normal modes, Rajan et al. (1987) showed that the perturbation of κ_n due to a small δc is

$$\delta\kappa_n = \int_0^\infty q_n \delta c dz \quad (10)$$

with

$$q_n = \frac{-\omega^2}{\bar{\kappa}_n} \frac{1}{\rho \bar{c}^3} \bar{Z}_n^2 \quad (11)$$

Note that the "static mode approximation" was also imposed in obtaining the eigenvalue perturbation equation. Finally, a substitution of (10) in (9) gives

$$\begin{aligned} \delta t_n^m = & \int_0^r \int_0^\infty \left\{ \frac{\partial q_n(r, z, \omega)}{\partial \omega} + \sum_m \frac{\partial}{\partial \omega} [f_{mn}(r, z, \omega) q_n(r, z, \omega) \right. \\ & \left. + g_{mn}(r, z, \omega) q_m(r, z, \omega)] \right\} \delta c(\vec{x}) dz dr \end{aligned} \quad (12)$$

Previously, Shang (1989) has developed a tomographic inverse technique based on adiabatic mode theory. His formula for modal travel time perturbation has only the first term in the integrand. Here, we have included the effects of mode coupling in the travel time change.

2.1.3 Optimal Inverse Solution

We represent δc in the vertical slice traversed by the rays and modes as a Fourier series, i.e.,

$$\delta c = \sum_{i=-I/2}^{I/2} \sum_{k=-K/2}^{K/2} a_{ijk} \exp[\sqrt{-1}(i\mathcal{K}_o x + k\mathcal{V}_o z)] \quad (13)$$

with

$$\mathcal{K}_o = \frac{2\pi}{\mathcal{X}} \quad (14)$$

$$\mathcal{V}_o = \frac{2\pi}{\mathcal{Z}} \quad (15)$$

where \mathcal{X} and \mathcal{Z} are the horizontal and vertical extents of the slice, respectively, and $(I + 1) \times (K + 1)$ is the total number of spectral components used. This truncated Fourier decomposition of δc is equivalent to gridding (i.e., discretizing) the physical space (x, z) into $(I + 1) \times (K + 1)$ points with a horizontal grid spacing of $\frac{\mathcal{X}}{I}$ and a vertical grid spacing of $\frac{\mathcal{Z}}{K}$. Using the Fourier decomposition, the inverse problem can be cast into simple linear algebra.

Putting the Fourier coefficients a_{ik} 's in a column vector, \underline{a} , and collecting all the measured ray travel time changes along resolved multipaths connecting sources and receivers in a column vector, $\underline{\delta t}^r$, the corresponding data-unknown relation becomes

$$\underline{\delta t}^r = \mathbf{G}^r \underline{a} + \underline{e}^r \quad (16)$$

where \mathbf{G}^r is the ray data kernel matrix, calculated by numerically integrating (2) for each of the Fourier components. Similarly, the data-unknown relation corresponding to the modes can be cast as

$$\underline{\delta t}^m = \mathbf{G}^m \underline{a} + \underline{e}^m \quad (17)$$

where the data vector $\underline{\delta t}^m$ contains the measured mode travel time changes and the mode data kernel matrix \mathbf{G}^m is computed from (12). In general, the data are contaminated by experimental noise, a combination of measurement and model errors. We represent the contamination in (16) and (17) by the noise vectors \underline{e}^r and \underline{e}^m , respectively.

There are several ways to derive the linear, minimum mean-square-error estimate, i.e., inverse solution (Cornuelle, 1985, and Chiu, 1985). Assuming

that \underline{a} , \underline{e}^r and \underline{e}^m have zero means and are uncorrelated, it can be shown that the minimum mean-square-error solution can be obtained by minimizing the following objective (or cost) function:

$$\begin{aligned} \mathcal{S}(\underline{a}) = & \frac{1}{2}(\underline{\delta t}^r - \mathbf{G}^r \underline{a})^T \mathbf{C}_e^r^{-1} (\underline{\delta t}^r - \mathbf{G}^r \underline{a}) \\ & + \frac{1}{2}(\underline{\delta t}^m - \mathbf{G}^m \underline{a})^T \mathbf{C}_e^m^{-1} (\underline{\delta t}^m - \mathbf{G}^m \underline{a}) \\ & + \frac{1}{2} \underline{a}^T \mathbf{C}_a^{-1} \underline{a} \end{aligned} \quad (18)$$

where \mathbf{C}_e^r , \mathbf{C}_e^m , and \mathbf{C}_a are the covariance matrices of \underline{e}^r , \underline{e}^m and \underline{a} , respectively. Furthermore, the error covariance of the solution is simply the inverse of the Hessian (the matrix of second derivatives) of \mathcal{S} (Chiu, 1985). One can see that the objective function is constructed by a combination of two data constraints (associated with rays and modes, respectively) and a statistical information constraint. It is worth mentioning that if \underline{e}^r , \underline{e}^m and \underline{a} had normal statistics, the minimum of (18) would coincide with the mode of the a posteriori distribution, which is the probability distribution function of \underline{a} , given $\underline{\delta t}^r$ and $\underline{\delta t}^m$. In such case, the minimum mean-square-error estimate and the mode of the a posteriori distribution estimate would be identical (Chiu, 1985).

The minimum mean-square-error inverse solution, $\hat{\underline{a}}$, and its error covariance, \mathbf{C}_ϵ , follow from the evaluations of the first and the second derivatives of \mathcal{S} with respect to \underline{a} . They are

$$\hat{\underline{a}} = \mathbf{C}_\epsilon (\mathbf{G}^{rT} \mathbf{C}_e^r^{-1} \underline{\delta t}^r + \mathbf{G}^{mT} \mathbf{C}_e^m^{-1} \underline{\delta t}^m) \quad (19)$$

$$\mathbf{C}_\epsilon = (\mathbf{G}^{rT} \mathbf{C}_e^r^{-1} \mathbf{G}^r + \mathbf{G}^{mT} \mathbf{C}_e^m^{-1} \mathbf{G}^m + \mathbf{C}_a^{-1})^{-1} \quad (20)$$

It is straight forward to go back to the physical space (x, z) from the

Fourier domain. The inverse solution for sound speed perturbation, $\hat{\delta c}$, and its error covariance are obtainable through applications of multi-dimensional discrete Inverse Fast Fourier Transforms (IFFT) to their Fourier-space counterparts. Ocean temperature perturbation is linearly proportional to sound speed perturbation. Thus, the calculation of temperature estimates from sound speed estimates is straight forward.

3 COASTAL OCEAN CIRCULATION MODEL FOR THE GULF OF SIRTE

3.1 The Model

A coastal primitive equation model with a fully active thermodynamics is developed for whole Mediterranean Sea (MED) based on the Princeton Ocean Model (POM) for the Gulf Stream (Mellor and Ezer, 1991). This is a three-dimensional MED model with a horizontal coastal-following, curvilinear nearly orthogonal and bottom-following, sigma, vertical coordinate system. The horizontal coastal-following, curvilinear nearly orthogonal model grid is designed using the EAGLEView software package developed at Mississippi State University (MSU). While the package allows for a high-resolution handling of the open boundary, coastlines and Gulf regions, a reduction of computational expense is still achieved (Ly *et al.*, 1993). The model has free surface dynamics and it uses a second order turbulence closure scheme for the mixed layer and a split mode time step. The model has one open boundary in the Atlantic ocean about 200 *km* west of the Strait of Gibraltar. Only the model sub-domain covering the Gulf of Sirte is used in this

data assimilation study. The average horizontal resolutions for the studied region is approximately 10 km.

The model equations governing the velocity, surface elevation, salinity, and temperature fields in the ocean have been described by Blumberg and Mellor (1983; 1987). The equations are written in a system of Cartesian coordinates with x eastward, y northward, and z upward. The free surface is located at $z = \eta(x, y, t)$ and the bottom is at $z = -H(x, y)$. The equations are

$$\frac{\partial \vec{U}}{\partial t} + \vec{U} \cdot \nabla \vec{U} + W \frac{\partial \vec{U}}{\partial z} + 2\vec{\Omega} \times \vec{U} = -\frac{1}{\rho_0} \nabla P + \frac{\partial}{\partial z} (K_m \frac{\partial \vec{U}}{\partial z}) + \vec{F} \quad (21)$$

$$\frac{\partial P}{\partial z} = -\rho g \quad (22)$$

$$\nabla \cdot \vec{U} + \frac{\partial W}{\partial z} = 0 \quad (23)$$

$$\frac{\partial \theta_i}{\partial t} + \vec{U} \cdot \nabla \theta_i + W \frac{\partial \theta_i}{\partial z} = \frac{\partial}{\partial z} (K_h \frac{\partial \theta_i}{\partial z}) + F_{\theta_i} \quad (24)$$

The density is computed using the equation of state (Mellor, 1991) in the general form

$$\rho = \rho_\theta(S, \theta, p) \quad (25)$$

The Coriolis force is denoted as $2\vec{\Omega} \times \vec{U}$, where $\vec{\Omega}$ is the earth rotation vector, \vec{U} is the horizontal velocity vector with components (U, V) , ∇ is the

horizontal gradient operator, ρ_o is the reference density, ρ is the in situ density, g is the gravitational acceleration, P is the pressure, K_m and K_h are the vertical turbulent exchange coefficients for momentum, and for heat and salt, respectively. In equation (24), θ_i may represent mean potential temperature, θ (or in situ temperature for shallow water application) or salinity, S . The potential density used here is an approximation, since it excludes the effects of pressure variations (Blumberg and Mellor, 1981). Here, $\vec{F}(F_x, F_y)$ in equation (21) and F_{θ_i} in equation (24) are the horizontal mixing terms (see Blumberg and Mellor, 1987).

The momentum conservation and diffusion equations (21) and (24) contain the vertical turbulent exchange coefficients which are determined by a second order turbulence closure scheme of Mellor and Yamada (1982). The turbulence scheme is characterized by equations for turbulent kinetic energy (TKE), $q^2/2$, and for the turbulent mixing length, ℓ . The two equations can be written in the same form (see Ly, 1992a), so that Q_i is either $q^2/2$ for TKE or $q^2\ell$ for the turbulent mixing length in the equation:

$$\frac{\partial Q_i}{\partial t} + \vec{U} \cdot \nabla Q_i + W \frac{\partial Q_i}{\partial z} = \frac{\partial}{\partial z} (K_q \frac{\partial Q_i}{\partial z}) + K_{mQ} [(\frac{\partial U}{\partial z})^2 + (\frac{\partial V}{\partial z})^2] + K_{hQ} \frac{g}{\rho_0} \frac{\partial \rho}{\partial z} - K_{hQ} \frac{q^3}{B_1} + F_Q \quad (26)$$

where

$$K_{mQ} = 2K_m, \quad K_{hQ} = 2K_h, \quad K_Q = 2/\ell, \quad F_Q = F_q \quad (27)$$

when Q_i represents $(q^2/2)$

and

$$K_{mQ} = \ell E_1 K_m, \quad K_{hQ} = \ell E_1 K_h, \quad K_Q = \widetilde{W}, \quad F_Q = F_\ell \quad (28)$$

when Q_i represents $(q^2\ell)$. Also in the above equations, \widetilde{W} is a "wall proximity" function (Mellor and Yamada, 1982) and B_1 is an empirical constant.

The first term on the right-hand side of (26) is the diffusion contribution, the next two terms represent shear production, the next is the buoyancy term, the next term represents dissipation, and the last represents the horizontal mixing. The vertical turbulent exchange coefficients (TEC) K_m, K_h , and K_q are defined as $K_m = \ell q S_m$, $K_h = \ell q S_h$, $K_q = \ell q S_q$ where S_m, S_h , and S_q are the stability functions (see Mellor, 1973; Mellor and Yamada, 1982).

At the free surface, $z = \eta(x, y)$, the surface wind stress, heat, and salinity fluxes are prescribed. At the bottom $z = -H(x, y)$, zero heat and salinity fluxes are used. Turbulent mixing length, ℓ , vanishes at the bottom. At land boundaries the condition of no diffusive fluxes of any property across the interface is used. Sigma coordinates can adequately model domains like the Gulf of Sirte with large bathymetric irregularities. Mode splitting of the barotropic and baroclinic modes are imposed in the model to save computer resources.

3.2 Model Parameters and Initialization

The Gulf of Sirte off Lybia is located in the southern middle part of the Mediterranean (MED). The region of interest in this study is bounded by latitudes 30 and 35 N and longitudes 15 and 22 E. The eastern part of the Gulf of Sirte is a deep region where the 100 – m isobath is less than 20 km from the coastline. The southern and western parts of the Gulf are considerably shallower. The bottom depths along the CAT sections used for

the assimilation are typically from 200 m to 2000 m .

In the model, the Gulf of Sirte and its surroundings have a horizontal resolution of about 10×10 km . There are 16 bottom-following (sigma) vertical levels with increased resolution in the mixed layer and lower resolution in the deeper layers. The external (barotropic) mode time step is 15 s , and the internal (baroclinic) one is 10 minutes, satisfying the Courant-Friedrichs-Levy (CFL) computational stability criterion. The model bathymetry is obtained from the global DBDB5 bathymetry dataset with $5' \times 5'$ resolution (National Geophysical Data Center, 1985) and is interpolated to the model grid. The bathymetry is filtered with a Shapiro (1970) filter to remove high frequency noise. The model is initialized with the Levitus temperature and salinity climatology (Levitus, 1982), and wind stress from the ECMWF (Ly *et al.*, 1992b) climatology. In all our computer simulation experiments, the model is spun up for 30 days diagnostically (temperatures and salinities held constant) before making the prognostic run.

3.3 Data Direct Insertion Technique

There are various data assimilation approaches. The simplest and the most computationally tractable is the direct insertion approach which is used in our investigation. In the following discussion of the direct insertion technique, we use superscripts f , o , and a to denote the forecast, observed, and analyzed (the best first guess) ocean fields, respectively. We also assume that CAT data is available at time intervals of Δt .

Generally, the ocean field predicted at time t , prior to the assimilation of

the data obtained at t , is related to the analyzed ocean field at time $t - \Delta t$ by

$$\mathbf{T}_t^f = \Gamma(\mathbf{T}_{t-\Delta t}^a) \quad (29)$$

where Γ is the mathematical operator describing the ocean dynamics, which in our cast is nonlinear. In the direct insertion method, the inserted data can be viewed as a "perturbation" introduced at a specific location $\{x_s, y_s, z_s\}$. We insert data at all time steps. The vector \mathbf{T} represents the discretized ocean variables such as velocity and temperature at the ocean model grid points. An observational vector can be thought of as consisting of a predicted and a perturbation part ε as:

$$\mathbf{T}_t^o = \mathbf{T}_t^f + \varepsilon \quad (30)$$

Then in the assimilation experiments we have

$$\Gamma(\mathbf{T}_{t-\Delta t}^a) = \mathbf{T}_t^o = \mathbf{T}_t^f + \varepsilon \quad (31)$$

at specific locations $\{x, y, z\} = \{x_s, y_s, z_s\}$. And

$$\Gamma(\mathbf{T}_{t-\Delta t}^a) = \mathbf{T}_t^f \quad (32)$$

at all other locations. Where ε is a difference between the predicted and observed value (a perturbation) and grows in time and space. It propagates and diffuses away from the CAT slice section. It is noted that the "true ocean" can be produced by replacing the predicted value \mathbf{T}_t^f with an observed \mathbf{T}_t^o at spatial and temporal resolutions which are dense and frequent enough to force the difference ε toward zero.

The analyzed field at time $t - \Delta t$ in the insertion experiments can be constructed by combining the forecast field and the observed field at $t - \Delta t$, that is

$$\mathbf{T}_{t-\Delta t}^a = (\mathbf{I} - \mathbf{W})\mathbf{T}_{t-\Delta t}^f + \mathbf{W}\mathbf{T}_{t-\Delta t}^o \quad (33)$$

where \mathbf{I} is an identity matrix and \mathbf{W} is a diagonal weighting matrix. The diagonal elements of \mathbf{W} consist of zeros and ones. The element is one if the corresponding model grid point is traversed by the CAT sections and if the corresponding variable is temperature. The element is zero otherwise. The construction of the analyzed field using equation (33) and the prediction of the forecast field using equation (29) is repeated at every data assimilation time step.

4 NUMERICAL EXPERIMENTS AND DISCUSSIONS

In addition to the model run that generated the "true ocean" (which will be referred as the TR experiment), four other model runs were performed. The latter runs will be referred as the EX_n experiments with $n = 0, 1, 2, 3$. EX_0 is an experiment with no data inserted. This experiment provides the baseline for judging improvements when data are inserted. In EX_1 (figure 10), the model was run with a single CAT section inserted daily. This CAT section has a northeast-southwest (NE-SW) orientation. In EX_2 (figure 17), a single CAT section was used again but, this time, the section has a northwest-southeast (NW-SE) orientation. In EX_3 , the model was run with the insertion of a total of five CAT sections. The five sections include the previous two diagonal slices as well as three other slices enclosing a coastal

volume making a CAT parallelogram (figure 24). These experiments are discussed in detail next.

4.1 The "True Ocean" Experiment *TR*

The scheme of the twin experiments in this study is shown in Table 1. The central issue is the convergence problem in using a fully nonlinear primitive equation coastal model with the direct data insertion technique. The global volume rms errors between the temperature fields of various experiments and the "true ocean" can be measures of the convergence in the domain studied.

The model is spun up for 30 days and then run for a year with ECMWF winds to produce the "true ocean" *TR*. One year is run to make sure the model "loses" the initial state (the loss of memory of the initial state). Figures 1, 2, and 3 show the "true ocean" temperature fields for day one at the surface (level 1), the mixed layer level (level 6), and the bottom level (level 15), respectively. Figures 4-6 show the "true ocean" temperature fields at the above levels for day 30. Hereafter, in the *TR* run, days 1 and 30 correspond to days 361 and 390, respectively. After one year of simulation the model is stable with the annual ECMWF winds. From figures 1 and 4 it is seen the SST fields are very slightly developing after 30 days (after one year of model simulation). The SST field in the shallow waters (the southern, southwestern, and southeastern regions of the Gulf) stay very much the same after 30 days of simulation. Temperatures in these regions are about 13 *deg C*. In the central and northern parts of the region, the SST field is slightly different. The region of 12 *deg C* has developed towards the northwest after 30 days

simulation. The colder water of the deeper layer has moved up to the surface by the mixing process in the central and northern parts (the deepest region of the MED with depths of about 4000 m).

Figures 2 and 5 show the temperature field of the "true ocean" at level 6 for one and 30 days, respectively. It is noted that level 6 of sigma coordinates corresponds to depths from the subsurface to 100 m . The temperature fields in all parts of the region stay very much the same after 30 days simulation. They have changed little compared to the surface level (figs 1 and 4). The temperature fields are almost identical at the bottom level (level 15) after 30 days simulation which are shown in Figures 3 and 6.

As expected, the 30-day run changes slightly the surface temperature field. In the deeper layers (levels 6 and 15), the temperature fields stay almost the same after the 30-day run.

4.2 The No Data Assimilated Experiment EX_0

The model is spun up for 30 days with Levitus temperature and salinity and ECMWF wind climatologies. The no data assimilated experiment EX_0 is performed by running the model for 30 days without the CAT data insertion. The temperature fields without data insertion at days one and 30 are shown in Figures 7 and 8, respectively. The temperature is developed after the 30-day run (Figure 8), but still close to the day one temperature when no data is inserted.

The effectiveness of the insertion of CAT data can be illustrated in Figure 9 which shows the global volume rms values of the differences between

this experiment without data assimilation and the comprehensive experiment with data insertion EX_3 . Figure 9 shows that at an initial time (day 1) the differences are very small. The differences are close to zero at day 1 because the temperature fields of EX_0 and EX_3 are the same at day zero. The fields are more different after more days of insertion. The growth of the global rms value of the differences must be understood as a "good sign" of the data insertion process. Here, the inserted data acts as an initial convergence factor to force the model to "lose" the initial state quickly and converge to the "true ocean" (see the experiments EX_1 , EX_2 and EX_3). The global rms differences grow very fast in the first ten days, slow down in the next ten days, and becomes stable at about day 30. A measure of the time scale for loss of predictability of the model is $Time_{predictability} = \sim 30$ days in the experiment EX_3 and other experiments (not shown).

4.3 The NE-SW Assimilation Experiment EX_1

The NE-SW CAT slice section can be seen in Figure 10 by a chain of 11 squares which has a distance of 300-350 *km*. The model is spun up for 30 days with temperature, salinity, and wind climatologies which are described above. Then the EX_1 experiment is performed by the insertion of CAT data for 30 days in the NE-SW slice at one day time step and at all levels. Figures 10-12 and 13-15 show the EX_1 temperature fields at the surface (level 1), mixed layer level (level 6), and the bottom level (level 15) for days one and 30, respectively. Comparing Figure 1 of the "true ocean" and Figure 10 of the NE-SW slice assimilated at the surface after one day of insertion, it

is seen that the two surface temperature fields are very different from each other, both in shallow and deep water. Here, the model accepts the CAT NE-SW data slice and spreads it out in both directions but more towards the east. Figure 13 shows the field after 30 days of assimilation. Figure 13 also shows the spreading is increased in the shallow water which may result from stronger mixing and horizontal shear and its interaction with topography. The stronger horizontal shear increases the horizontal diffusion [terms \vec{F} and F_{θ_i} in equations (21) and (24)]. This is made clearer by comparing Figure 14 of day 30 assimilation at level 6 with Figure 2 of the "true ocean" at the same level. Here, the CAT data from the NE-SW assimilated slice is accepted by the model and is spread out towards the southeast where the Gulf has shallower average depths. In the bottom layer the Figure 6 of the "true ocean" and the Figure 15 of the NE-SW assimilation are very much the same.

The convergence of the NE-SW CAT slice assimilation experiment towards the "true ocean" can be measured by the global rms-error over a volume of the entire domain studied. Figure 16 shows the rms-error between the "true ocean" and the NE-SW slice experiment EX_l for 30 days of assimilation. The rms-errors are 0.95, 0.925, and 0.64 for days 0, 1, and 30, respectively. This means that the rms-errors of the NE-SW slice assimilation decrease 3 and 33 % after one day and 30 days of assimilation. The model and assimilation scheme work very well in this case. The rms-error curve is almost linear and it is expected that the convergence to the "true ocean" would be even better if the insertion were made more often and at higher horizontal and vertical spatial resolution.

4.4 The NW-SE Assimilation Experiment EX_2

This experiment is very similar to the NE-SW CAT slice above. The NW-SE CAT slice can be seen in Figure 17 by a chain of 11 squares over a distance of 300-350 *km*. In this experiment, the model is spun up for 30 days with the Levitus temperature and salinity, and the ECMWF wind climatologies. Then the model is run for 30 days with the CAT data insertion along the NW-SE slice at one day time interval for all levels (16 level) to perform the assimilation experiment EX_2 .

Figures 17-19 and 20-22 show the EX_2 temperature fields at the level 1 (surface), level 6 (mixed layer), and level 15 (bottom layer) for days 1 and 30, respectively. In general, it is seen from these figures that temperature fields are developing towards the "true ocean". As in the experiment EX_1 , comparing Figure 1 of the "true ocean" and Figure 17 of the NW-SE slice assimilated at the surface, shows that the two surface temperature fields are very different from each other everywhere in the region. The surface temperature field after 30 days of CAT assimilation is shown in Figure 20. It is seen that the model accepts the CAT slice data and spreads it out along both sides of the NW-SE section at the surface. It is clear from Figure 5 of the "true ocean", Figure 18 of day one, and Figure 21 of day 30 that at level 6 the temperature of the NW-SE slice is shifted and more spread out northwards in the mixed layer. As mentioned in the EX_1 , this may be the result of the strong horizontal shear in the NW-SE slice region which increases the horizontal diffusion [terms \vec{F} and F_θ in equations (21) and (24)]. In the bottom layer the temperature fields of the "true ocean" at day

30 in Figure 6 and of the NW-SE slice assimilation experiment EX_2 at day 30 in Figure 22 are very much the same.

The convergence of the temperature field to the "true ocean" in the NW-SW CAT slice experiment EX_2 can be measured by rms-errors in Figure 23. This figure shows the global rms-error over the volume of the entire domain between the "true ocean" and the the NW-SE slice experiment EX_2 . It is interesting to note that the global rms-errors of EX_1 and EX_2 have nearly the same distribution for 30 days of assimilation which are 0.95, 0.925, and 0.065 for days 0, 1, and 30, respectively. As in EX_1 , the rms-errors of the NW-SE experiment decrease 3 and about 33 % after one day and 30 days of assimilation, respectively. One of the reasons for the similarity in the two rms-error distributions is that two slices (NE-SW and NW-SE) have the same length (300-350 km) and are very symmetric. As in the experiment EX_1 , the model and the assimilation scheme work very well together in this case. The model is greatly improved (33 %) after 30 days of CAT insertion. It is also seen that the behavior of the global rms-errors is nearly insensitive to the change in the CAT data section location in energetic regions of the Gulf in the experiments EX_1 and EX_2 . These two slices have almost the same effectiveness in improving the model errors on the global space scale. These experiments also show that the internal forcing provided by the single slice of inserted CAT data is not localized in physical space in inducing immediate correlation between the fully nonlinear primitive equation model and the "true ocean". This result is very different from the results of Malanotte-Rizzoli and Holland (MRH, 1988) who found that the single section of inserted data is too localized in physical space to induce any immediate correlation between a QG model and

the reference ocean. The reason for these different results is the differences not only in data and models used, but also in our smaller coastal domain. The rms-error curve is almost linear in this case and it is expected that the convergence to the "true ocean" will be better if the temporal and spatial resolutions of the CAT insertion is higher.

4.5 The Combined Slices Assimilation Experiment EX_3

The more comprehensive experiment is EX_3 which is more realistic for coastal acoustic tomography. The combined slices in experiment EX_3 include the EX_1 slice and EX_2 slice together and three other CAT slices. All these slices together make a parallelogram without the southern side. The EX_1 and EX_2 slices are two diagonals of this CAT parallelogram which is seen in Figure 24. The lengths of the western and eastern sides of the parallelogram (which will be called LON LEFT and LON RIGHT) are about 200 km, and the length of the northern side (which will be called LAT slice) is about 250 km. As in two previous experiments, the model is spun up for 30 days with the Levitus temperature, salinity, and ECMWF wind climatologies. Then the CAT data is inserted into the model, as described in the scheme (31) and (32), for 30 days at one day time intervals and at 16 levels to perform the combined slices assimilation experiment EX_3 .

The temperature fields of the combined CAT slices after one day of assimilation at the surface (level 1), the mixed layer level (level 6), and the bottom levels (level 15) are shown in Figures 24-26. Figures 27-29 show the temperature fields of the above levels for day 30. It is seen from these figures

that the temperature fields of all levels at day one are very "far" from the "true ocean". As in two other experiment, the temperature fields in this experiment of levels 1 and 5 are closer to each other than to the fields of the bottom layer. This is a result of the surface layer and the mixed layer levels being much closer with stronger mixing, especially in shallow water. After 30 days of the combined slices assimilation, the temperature at the surface (Figure 27) is spread out in all directions, but stronger in the southeastern corner and in the southern part of the region where the water is shallower. The mixing, horizontal diffusion, nonlinearity, and interaction with topography play an important role in the advection process of temperatures. At day 30 the SST field of this experiment (Figure 27) converges well to the "true ocean" of Figure 4. It is seen in all three experiments that the temperatures of the mixed layer level (Figures 14, 21 and 28) at day 30 converge very well to the "true ocean" in comparison with the surface levels. This results from the fact that the mixing is strongest inside the mixed layer where the vertical turbulence has the largest activity. The turbulence exchange coefficients K_m and K_h in (21) and (24) have maximum values inside mixed layers and minimum values at the surface (see Ly, 1991). Inside the mixed layer both "top down" and "bottom up" processes must be active while only the "bottom up" process is active at the surface. These processes are important in our cases because of the CAT data insertion by vertical slices. The temperature field at level 15 after 30 days of assimilation in Figure 29 is almost identical with the "true ocean" in Figure 6.

The convergence temperatures can be seen in Figure 30 which shows the global rms-error over a volume of the entire domain between the "true ocean"

and the the temperature in this experiment EX_3 . As expected, the convergence of the temperature field to the "true ocean" is best in this experiment in comparison with the two experiments above. The rms-errors drop dramatically in the first ten days of assimilation from 0.92 to 0.72 *deg C*. This makes the convergence to the "true ocean" of 22 % after the first ten days of assimilation. The rms-errors drop slower in the next 10 days from 0.72 at day 10 to 0.59 at day 20. The convergence in this second ten days of assimilation is 18 %. In the last ten days of assimilation the rms-errors drop slowest from 0.59 to 0.50 at day 30 which makes the convergence of 15 %. Totally, the global rms-errors drop is about 50 % after 30 days of data insertion. The model and the assimilation scheme work very well together. This shows that inserting the "right" data into a "wrong" model tends to drive the "wrong" model closer to the "truth" and to reduce global rms-errors. The inserted CAT data acts as an initial convergence maker in the model. This convergence grows very fast. After 30 days of insertion the convergence is increased by almost 50 %. This also shows that the "true ocean" and the model with CAT data insertion are strongly correlated. As in the two above experiments, the rms-error curve is very close to linear and it is expected the convergence to the "true ocean" will be better if the temporal and spatial resolution of the CAT insertion is higher. It is interesting to note that convergence are not proportional to the number of CAT slice sections in an experiment. The experiment EX_1 has a convergence of 33 %; EX_2 has a convergence about 33 %, but EX_3 has about 50 %).

It is interesting to see the convergence of this experiment EX_3 to the "true ocean" after another 30 days of data insertion. Figure 31 shows the

temperature field at the mixed layer level (level 6) at day 60 in comparison with the "true ocean" at this day. The temperature converges significantly to the "true ocean" at day 60. The temperature fields at this level are almost identical. The rms-error distribution for days between 31 and 60 is shown in Figure 32. The rms-errors between the "true ocean" and the temperature field of this experiment are reduced by 17 % after 30 days (31-60) of insertion. Totally, after 60 days of CAT data insertion the rms-errors are reduced by 66 %. The model is improved by 66 % after 60 days of assimilation.

Three other assimilation experiments with CAT insertions along the northern (LAT), western (LON LEFT) and eastern (LON RIGHT) sides of the above parallelogram (Figure 24) have been carried out to study the effectiveness of various local slices. The model spreads these CAT slices out differently, and this strongly depends on the horizontal diffusion, mixing process, and nonlinear interaction with topography. At the surface, after 30 days of assimilation the LAT slice is spread out along both sides, but more towards the north (not shown). The LON LEFT slice is spread out greater in the northern part towards the east, after 30 days (not shown). And at the surface the LON RIGHT slice, after 30 days, is spread out greater in the middle towards the west (not shown). Although these CAT slices have various temperature advection, but the their global rms-errors distributions are almost the same (not shown). Their rms-errors are reduced by 27 % after 30 days of assimilation. These experiments confirm that there is no most effective slice between different CAT slice sections. All slices have almost the same "weight" in forcing the coast model in converging to the "true ocean".

5 SUMMARY

Coastal acoustic tomographic (CAT) data is used in "twin" experiments by direct data insertion. A series of assimilation experiments has been carried out and discussed in which data are inserted along various CAT slices into a coastal ocean primitive equation model for the Gulf of Sirte. The model is developed for the whole Mediterranean (MED) Sea and is used for studying a direct insertion technique. The model has realistic coastlines and topography. This model also has a coastal-following, curvilinear, nearly orthogonal horizontal coordinate system, fully active thermodynamics, a second order turbulence closure, 16 bottom-following, sigma vertical levels, and an average resolutions of about 10 by 10 *km*. The model was spun up for 30 days with Levitus temperature and salinity and ECMWF wind climatologies and then run for a year to generate the "true ocean". In the assimilation experiments, after a 30-day spinup, the model was run for 30 days with an insertion time interval of one day at all 16 vertical levels (except the comprehensive experiment *EX₃* which was run for 60 days).

The results indicate that the model works well with the assimilation scheme to accept data slices and spread it out nearly in all directions in the Gulf of Sirte. The inserted data acts as an initial convergence maker which forces the model to "lose" the initial state quickly and converge to the "true ocean". The global rms-errors in the studied domain between the "true ocean" and the temperature fields of the comprehensive experiment *EX₃* decrease by about 50 % after 30 days and 66 % after 60 days of assimilation. The rms-errors of two other experiments with diagonal slices are

reduced by 33 %, and of all other sides of the parallelogram are reduced by 27 % after 30 days of insertion. This shows that inserting the "right" data into a "wrong" model tends to drive the "wrong" model closer to the "truth" and to reduce global rms-errors. The good convergence also shows that the "true ocean" and the model with CAT data insertion are strongly correlated. The rms-error curve is very close to linear in the 30 days of insertion. Then, it is expected that the convergence to the "true ocean" will be better if the temporal and spatial resolutions of the CAT insertion are higher.

The temperature is spread out greater in the shallow water which may be the result of stronger mixing and horizontal shear and its interaction with topography, which increases horizontal diffusion. It is seen in all experiments that the temperatures of the mixed layer level at day 30 converge very well to the "true ocean" in comparison with the surface levels. This results from the fact that the mixing is strongest inside mixed layers. The turbulence activities are strongest inside mixed layers and weakest at the surface. Inside mixed layers both "top down" and "bottom up" processes must be active while only the "bottom up" process is active at the surface. These processes are important in CAT data assimilation because of insertions by vertical slices.

The behavior of the global volume rms-errors is nearly insensitive to the change of the CAT data slice location in the more energetic regions of the Gulf. Although side-slices and diagonal-slices of the parallelogram have various temperature advection, their global rms-errors distributions are almost the same. Their rms-errors are reduced by 27 % and 33 % after 30 days of assimilation. There is no the most effective slice between different local CAT

slices. All slices have almost the same "weight" (effectiveness) in improving the model errors on the global space scale of the Gulf of Sirte. The convergence is not proportional to the number of CAT slices in an experiment.

The experiments also show that the internal forcing provided by the single slice of inserted CAT data induces an immediate correlation between the fully nonlinear primitive equation model and the "true ocean" that is not localized in physical space. This result is very different from that of Malanotte-Rizzoli and Holland who found that the single section of inserted data is too localized in physical space to induce any immediate correlation between a QG model and the reference ocean (MRH, 1988). The reason for our different conclusions is due to the data and models used and to our smaller coastal domain.

Overall, a direct insertion scheme for CAT data works very well with a coastal multilevel, primitive equation model with complete thermodynamics, a second order turbulence closure, and realistic coastlines and topography. A comparison of this scheme with a modified Kalman filter using CAT is recommended for future investigation.

REFERENCES

Blumberg, A. F. and Mellor, G. L. 1987. A description of a three dimensional coastal ocean circulation model. *Three Dimensional Coastal Models*, Coastal and Estuarine Sciences, 4, N. S. Heaps, editor, AGU Geophysical Monograph Board, 1-16.

Blumberg, A. F. and Mellor, G. L. 1983. Diagnostic and prognostic numerical circulation studies of the South Atlantic Bight. *J. Geophys. Res.*, **88**, 4579-4592.

Blumberg, A. F. and Mellor, G. L. 1981. A numerical calculation of the circulation in the Gulf of Mexico, Dynalysis of Princeton, Report No. 66.

Blumberg, A. F. and Herring, J. 1987. Circulation modeling using orthogonal curvilinear coordinates, In: J. C. J. Nihoul and B. M. Ramart, editors, *Three Dimensional Models of Marine and Estuarine Dynamics*, Elsevier Oceanography Series, **45**, Amsterdam, 55-88.

Chiu, C. -S. 1985. Estimation of planetary wave parameters from the data of the 1981 Ocean Acoustic Tomography Experiment. MIT/WHOI Ph.D. Thesis.

Chiu, C-S., J.H. Miller, and J.F. Lynch, "Inverse Techniques for Coastal Acoustic Tomography," Proceedings of the 1993 International Conference on Theoretical and Computational Acoustics, 1993, accepted.

Cornuelle, B. C. Wunsch, C. Behringer, D. Birdsall, T. Brown, M. Heinmiller, R. Knox, R. Metzger, K. Munk, W. Spiesberger, J. Spindel, R. Webb, D. and Worcester, P. 1985. Tomographic maps of the ocean mesoscales, I, Part 1. *J. Phys. Oceanogr.*, **15**, 133–152.

Desaubies, Y. Chiu, C. -S. and Miller, J. H. 1986. Acoustic mode propagation through a range-dependent ocean. *J. Acoust. Soc. Am.*, **80**, (4), 1148–1160.

Ezer, T. and Mellor, G. L. 1992. A numerical study of the variability and the separation of the Gulf Stream, induced by surface atmospheric forcing and lateral boundary flows. *J. Phys. Oceanogr.*, **22**, 660– 682.

Ghil, M. and Malanotte-Rizzoli, P. 1991. Data Assimilation in Meteorology and Oceanography. *Advances in Geophys.*, **33**, 141–266.

Hellerman, S. and Rosenstein, M. 1983. Normal monthly wind stress over the world ocean with error estimates. *J. Phys. Oceanogr.*, **13**, 1093–1104.

Hurlburt, H. E. 1986. Dynamic transfer of simulated altimeter data into subsurface information by a numerical ocean model. *J. Geophys. Res.*, **91**, 2372–2400.

Kalman, R. E. 1960. A new approach to linear filtering and prediction problems. *J. Basic Eng.*, **82D**, 35–45.

Kindle, J. G. 1986. Sampling strategies and model assimilation of altimetric data for ocean monitoring and prediction. *J. Geophys. Res.*

91, 2418–2432.

Levitus, S. 1982. *Climatological atlas of the world ocean*. National Oceanic and Atmospheric Administration. Professional Paper No. 13, U.S. Government Printing Office, Washington D. C., 173 pp.

Ly, N. L. 1991. An application of the E - ϵ turbulence model for studying coupled air-sea boundary layer structure. *Boundary-Layer Meteorol.*, **54**, 327–346.

Ly, N. L. and Kantha, L. H. 1993. A numerical study of the nonlinear interaction of Hurricane Camille with the Gulf of Mexico Loop Current. *Oceanologica Acta*, **16**, 4, 341–348 .

Ly, N. L., Luong, P. and Chiu, C. S. 1993. Application of grid generation technique in coastal ocean modeling for the Mediterranean Sea. *EOS*, **O12B-4**, American Geophysical Union, Fall Meeting,

Ly, N. L. 1992a. The Gulf of Mexico response to Hurricane Frederic simulated with the Princeton numerical ocean circulation model. *Technical Rept.*, **TR-2**, Institute for Naval Oceanography, 42 pp.

Ly, N. L., Kindle, J. C., Thompson, J. D. and Youtsey, W. J. 1992b. Wind stress analysis over the Western Equatorial Pacific and North Atlantic Oceans based on ECMWF operational wind products 1985–1989. *Technical Rept.*, **TR-3**, Institute for Naval Oceanography, 110 pp.

- Malanotte-Rizzoli, P. and Holland, W. R. 1986. Data constraints applied to models of the ocean general circulation. Part I: The steady case. *J. Phys. Oceanogr.*, **16**, 1665–1682.
- Malanotte-Rizzoli, P. and Holland, W. R. 1988. Data constraints applied to models of the ocean general circulation. Part II: The transient, eddy-resolving case. *J. Phys. Oceanogr.*, **18**, 1093–1107.
- Mellor, G. L. 1991. An equation of state for numerical models of oceans and estuaries. *J. Atmos. Oc. Tech.*, **8**, 6, 609–611.
- Mellor, G. L. 1973. Analytic prediction of the properties of stratified planetary surface layer. *J. Atmos. Sci.*, **30**, 1061–1069.
- Mellor, G. L. and Ezer, T. 1991. A Gulf Stream model and an altimetry assimilation scheme. *J. Geophys. Res.*, **96**, 8779–8795.
- Mellor, G. L. and Yamada, T. 1982. A hierarchy of turbulence closure models for planetary boundary layers. *J. Atmos. Sci.*, **31**, 1791–1896.
- Miller, J.H., C-S. Chiu, and J.F. Lynch, "Signal Processing for Coastal Acoustic Tomography," Proceedings of the 1993 International Conference on Theoretical and Computational Acoustics, 1993, accepted.
- National Geophysical Data Center (1985) Worldwide Gridded Bathymetry DBDB5 5-minute Latitude/Longitude Grid, Data Announcement 85-MGG-01, NOAA/NGDC, Boulder, CO.

Malanotte-Rizzoli, P. and Holland, W. R. 1986. Data constraints applied to models of the ocean general circulation. Part I: The steady case. *J. Phys. Oceanogr.*, **16**, 1665–1682.

Malanotte-Rizzoli, P. and Holland, W. R. 1988. Data constraints applied to models of the ocean general circulation. Part II: The transient, eddy-resolving case. *J. Phys. Oceanogr.*, **18**, 1093–1107.

Mellor, G. L. 1991. An equation of state for numerical models of oceans and estuaries. *J. Atmos. Oc. Tech.*, **8**, 6, 609–611.

Mellor, G. L. 1973. Analytic prediction of the properties of stratified planetary surface layer. *J. Atmos. Sci.*, **30**, 1061–1069.

Mellor, G. L. and Ezer, T. 1991. A Gulf Stream model and an altimetry assimilation scheme. *J. Geophys. Res.*, **96**, 8779–8795.

Mellor, G. L. and Yamada, T. 1982. A hierarchy of turbulence closure models for planetary boundary layers. *J. Atmos. Sci.*, **31**, 1791–1896.

Miller, J.H., C-S. Chiu, and J.F. Lynch, "Signal Processing for Coastal Acoustic Tomography," Proceedings of the 1993 International Conference on Theoretical and Computational Acoustics, 1993, accepted.

National Geophysical Data Center (1985) Worldwide Gridded Bathymetry DBDB5 5-minute Latitude/Longitude Grid, Data Announcement 85-MGG-01, NOAA/NGDC, Boulder, CO.

Rajan, S. Lynch, J. F. and Frisk, G. V. 1987. Perturbative inversion methods for obtaining bottom geo parameters in shallow water. **82**, 998–1017.

Shang, E. C. 1989. Ocean Acoustic Tomography based on adiabatic mode theory. *J. Acoust. Soc. Am.*, **85**, (4), 1531–1537.

Shapiro, R. 1970. Smoothing, filtering, and boundary effects.

Smagorinsky, J. 1963. General circulation experiments with the primitive equations. Part I. The basic experiment. *Monthly Weather Review*, **91**, 99–164.

Thompson, J. D. 1986. Altimeter data and geoid error in mesoscale ocean prediction: some results from a primitive equation model. *J. Geophys. Res.*, **91**, 2401–2417.

Von Der Heydt, K. Kemp, J. Lynch, J. F. Miller, J. H. and Chiu, C. -S. 1992. Shallow Water Tomography in the Barents Sea using LAN Telemetry. *Woods Hole Oceanographic Institution Technical Report*, October.

7 Figure Captions

Table 1 Block diagram of the simulation twin experiments for studying coastal acoustic tomography data assimilation.

Fig. 1 Temperature field of the "true ocean" at the sea surface (level 1) on day 1.

Fig. 2 Same as figure 1, but for level 6 (a mixed layer level).

Fig. 3 Temperature field of the "true ocean" on day 1 for level 15 (the bottom layer).

Fig. 4 Temperature of the "true ocean" at the sea surface (level 1) on day 30.

Fig. 5 Same as Fig. 4 but for level 6.

Fig. 6 The "true ocean" at level 15 (the bottom layer) on day 30.

Fig. 7 Temperature of the sea surface for day 1 in the experiment EX_0 with no data assimilated.

Fig. 8 Same as Fig. 7 but for day 30.

Fig. 9 Root-mean-square (rms) values of the differences between the experiment with the insertion of five CAT slices (EX_3) and the experiment without data insertion (EX_0).

Fig. 10 Temperature at the sea surface on day 1 of the experiment EX_1 with a single NE-SW tomographic section. The tomographic section can be seen as a chain of 11 squares.

Fig. 11 Same as Fig. 10 but for level 6 (a mixed layer level).

Fig. 12 Same as Fig. 10 but for level 15 (bottom layer)

Fig. 13 Temperature at the sea surface for day 30 of the experiment EX_1 with a single NE-SW tomographic section.

Fig. 14 Same as Fig. 13 but for level 6.

Fig. 15 Same as Fig. 13 but for level 15.

Fig. 16 Global volume rms error versus time for a period of 30 days between the nowcast temperature fields in EX_1 and the "true ocean" temperature fields.

Fig. 17 Temperature at the sea surface (level 1) on day 1 of the experiment EX_2 with a single NW-SE tomographic section. The tomographic section can be seen as a chain of 11 squares.

Fig. 18 Same as Fig. 17 but for level 6 (a mixed layer level).

Fig. 19 Same as Fig. 17 but for level 15 (bottom layer).

Fig. 20 Temperature at the sea surface on day 30 in EX_2 with a NW-SE tomographic section.

Fig. 21 Same as Fig. 20 but for level 6.

Fig. 22 Same as Fig. 20 but for level 15.

Fig. 23 Global volume rms error versus time for a period of 30 days between the nowcast temperature fields in EX_2 and the "true ocean" temperature fields.

Fig. 24 Day-1 sea surface temperature of the comprehensive experiment EX_3 with five tomographic sections forming a parallelogram enclosing a coastal region. The parallelogram (without a southern section) can be seen as five chains of brightened squares.

Fig. 25 Same as Fig. 24 but for level 6.

Fig. 26 Same as Fig. 24 but for level 15.

Fig. 27 Sea surface temperature on day 30 in the experiment EX_3 with the assimilation of five tomographic sections.

Fig. 28 Same as Fig. 27 but for level 6.

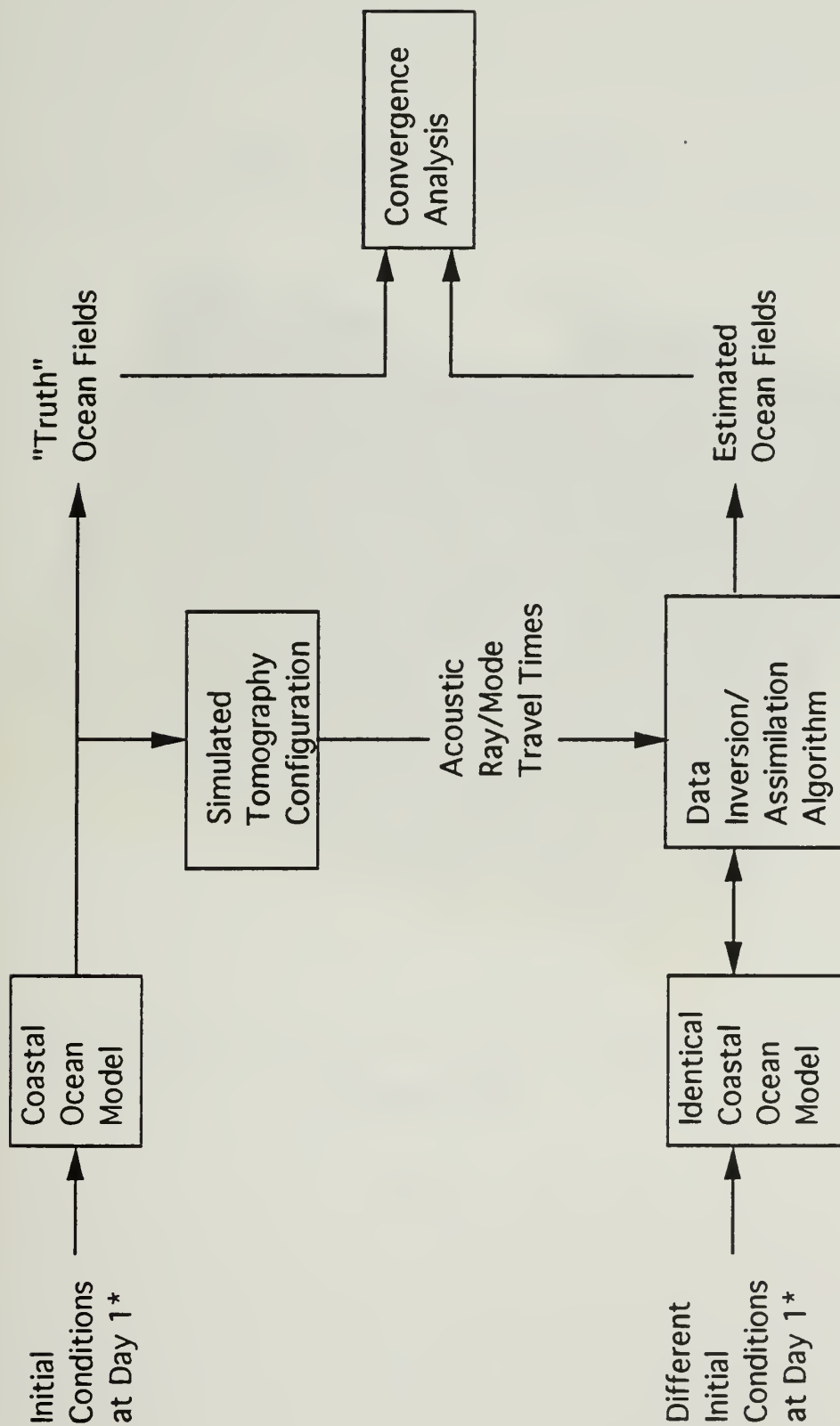
Fig. 29 Same as Fig. 27 but for level 15.

Fig. 30 Global volume rms error versus time for a period of 30 days between the nowcast temperature fields in EX_3 and the "true ocean" temperature fields.

Fig. 31 Temperature at a mixed layer level (level 6) in the comprehensive experiment EX_3 right after 60 days of data insertion. Temperature of the "true ocean" for the same time (i.e., day 60) and same level is shown in the lower panel.

Fig. 32 Global volume rms error versus time from day 31 to day 60 between the nowcast temperature fields in EX_g and the "true ocean" temperature fields.

Twins Experiments



Tab 1

* Day 1 is the beginning of the data assimilation period

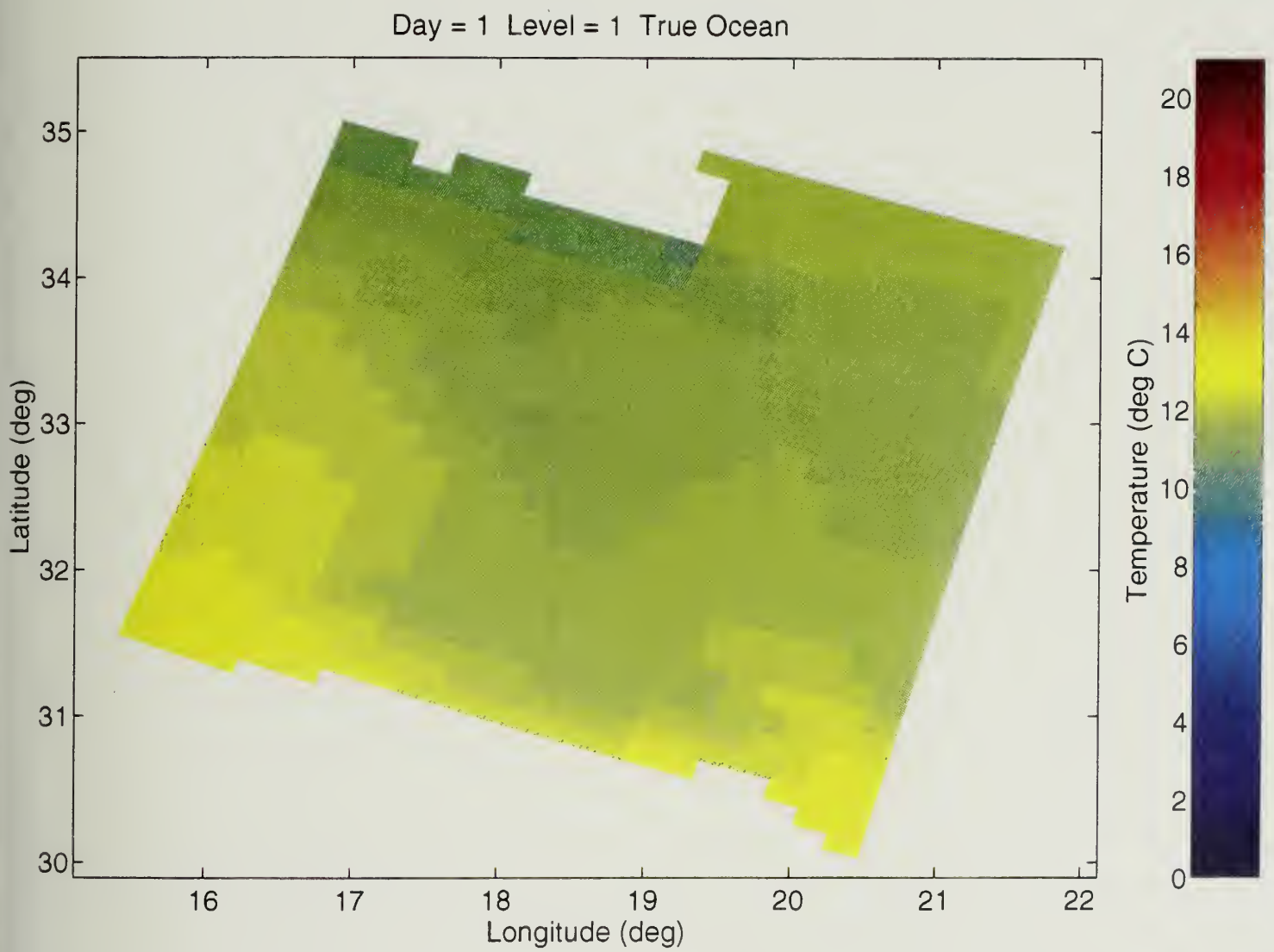


Fig. 1

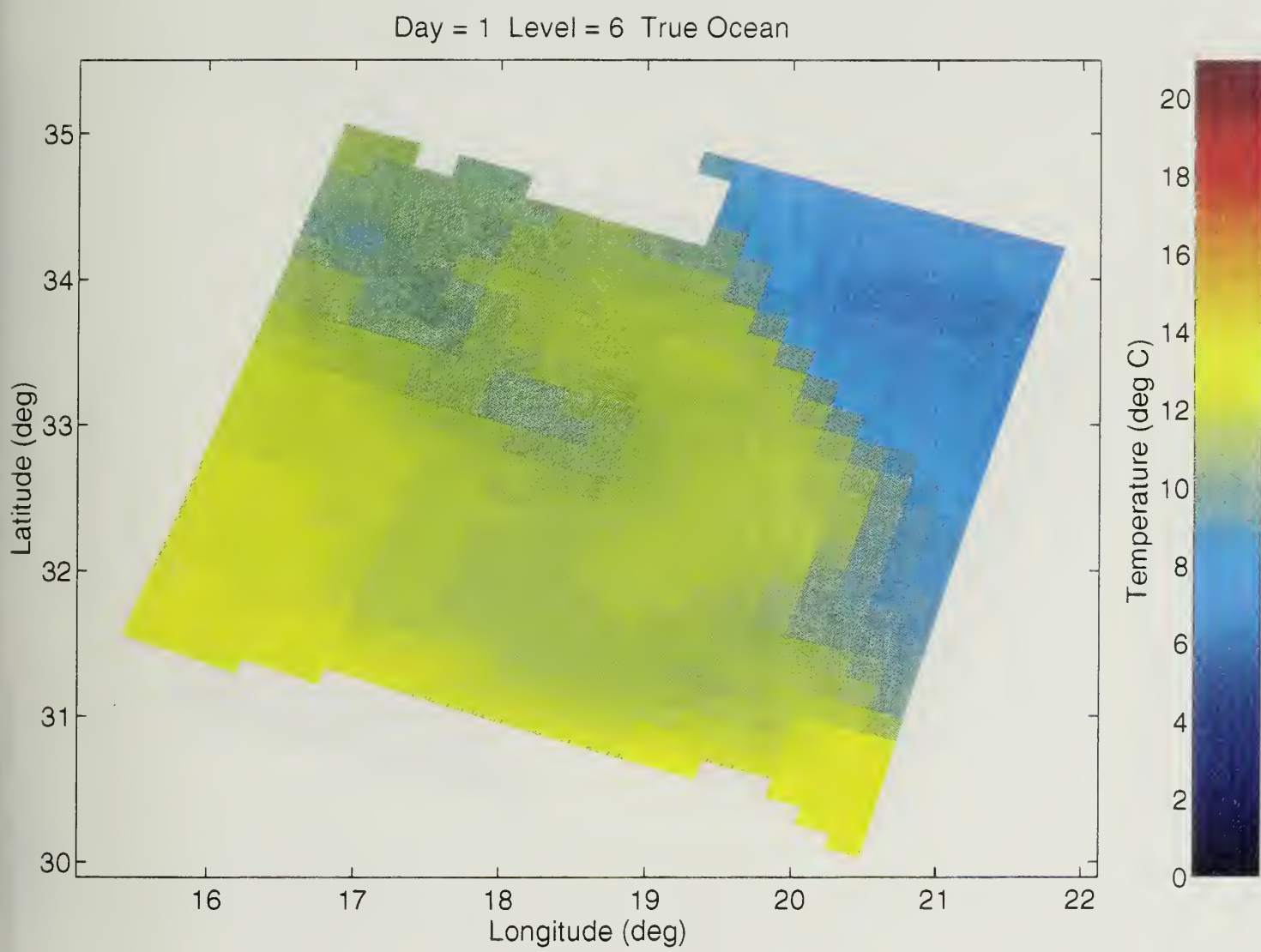
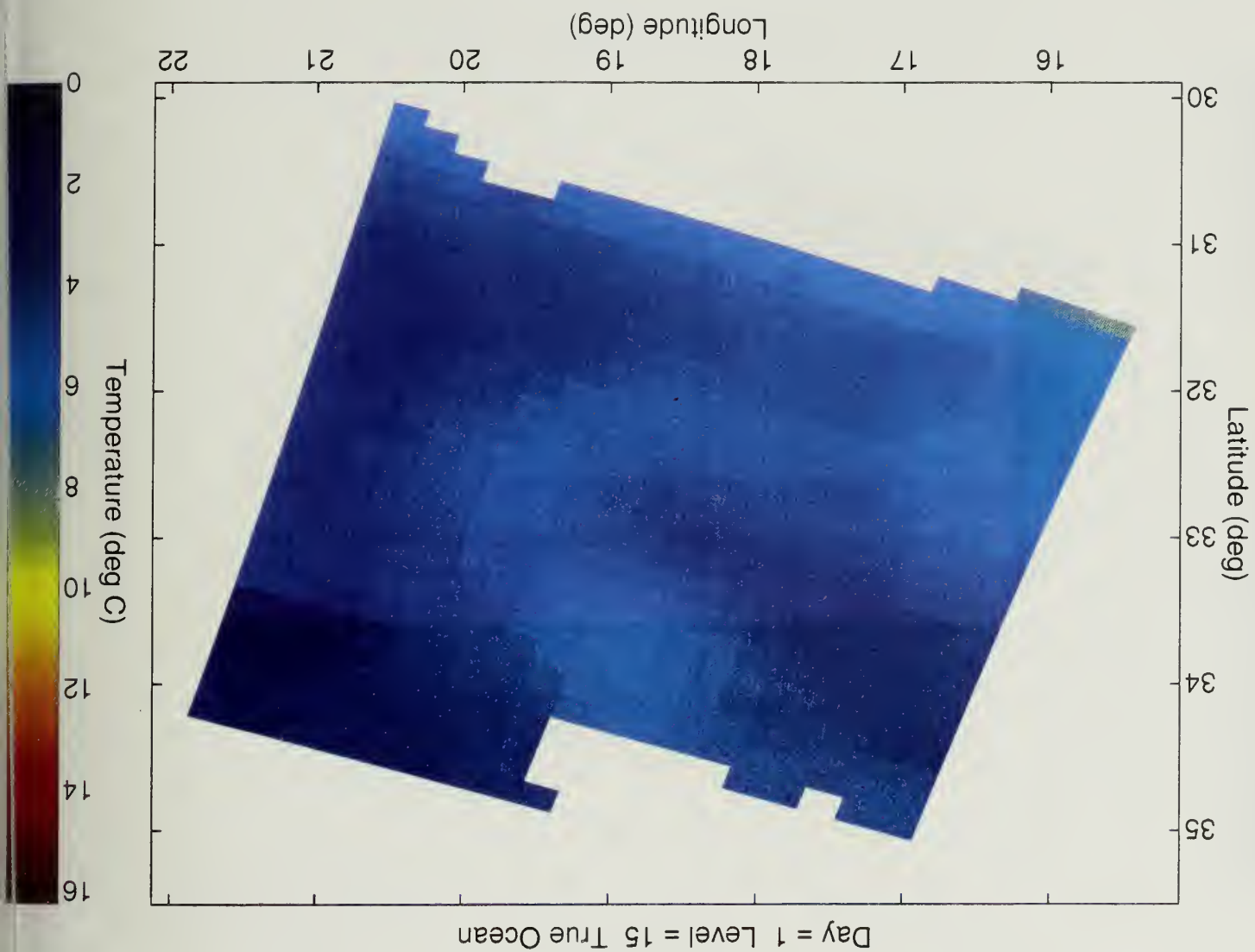


Fig. 2

Fig. 3



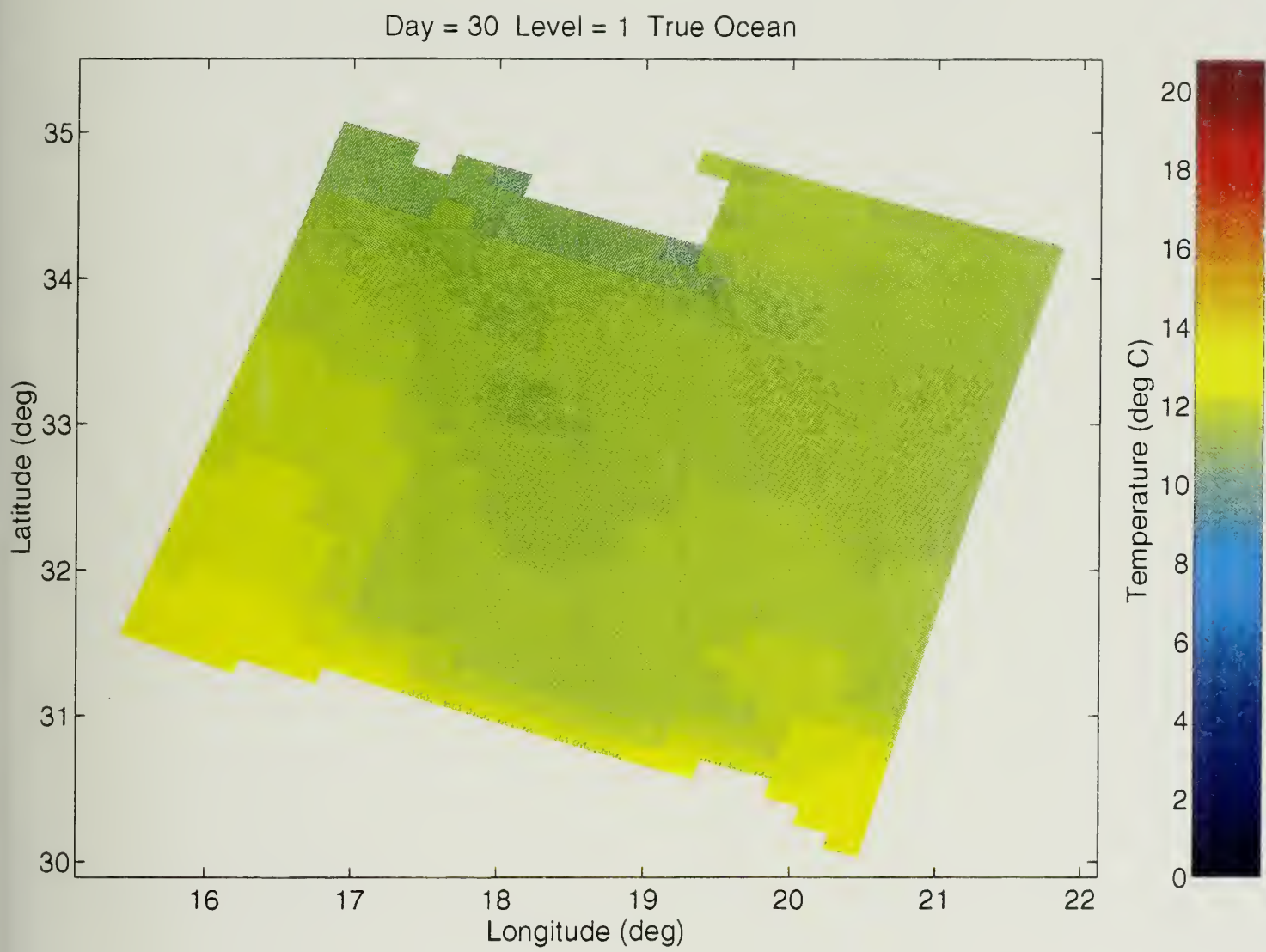


Fig. 4

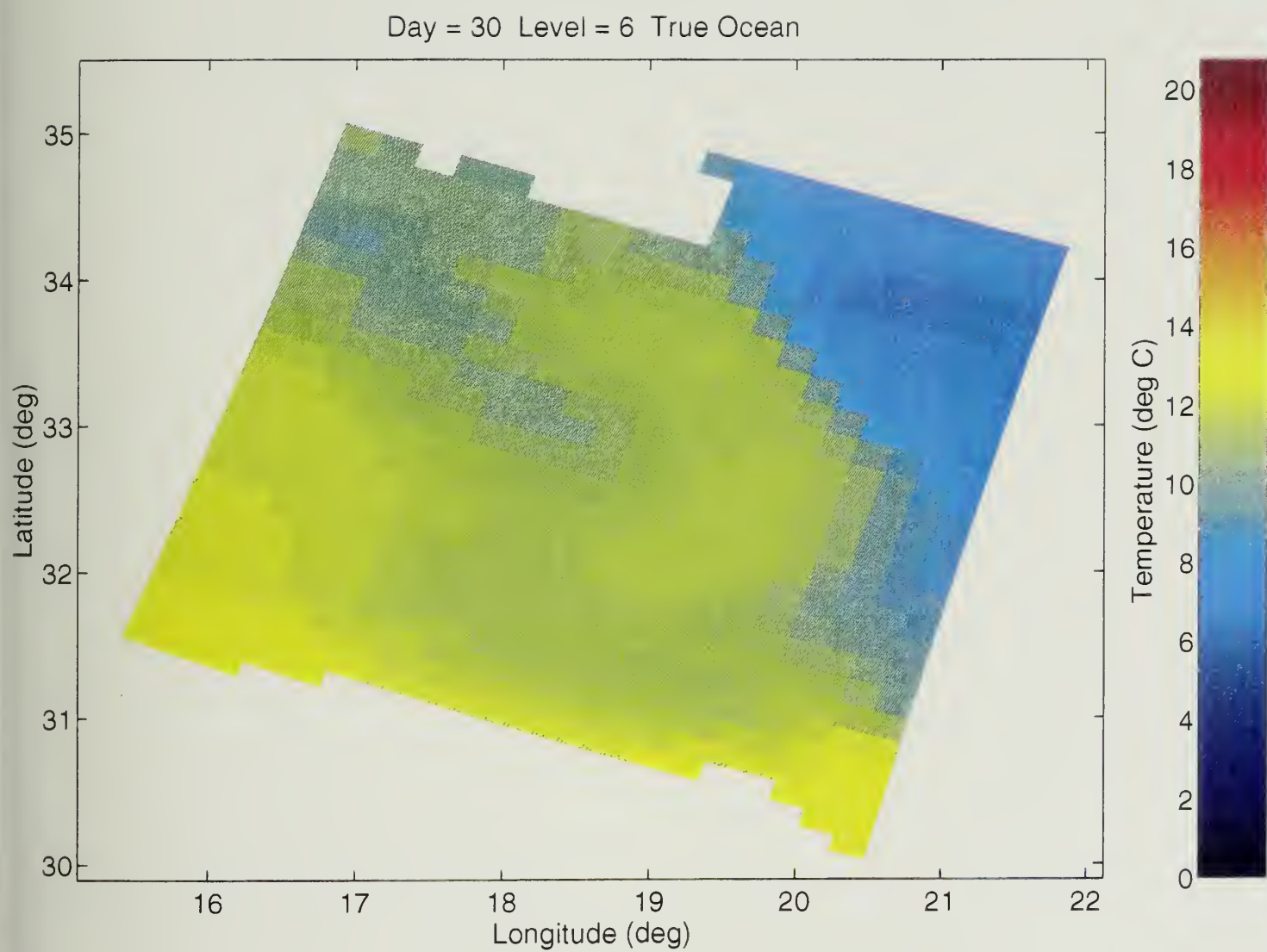


Fig. 5

Day = 30 Level = 15 True Ocean

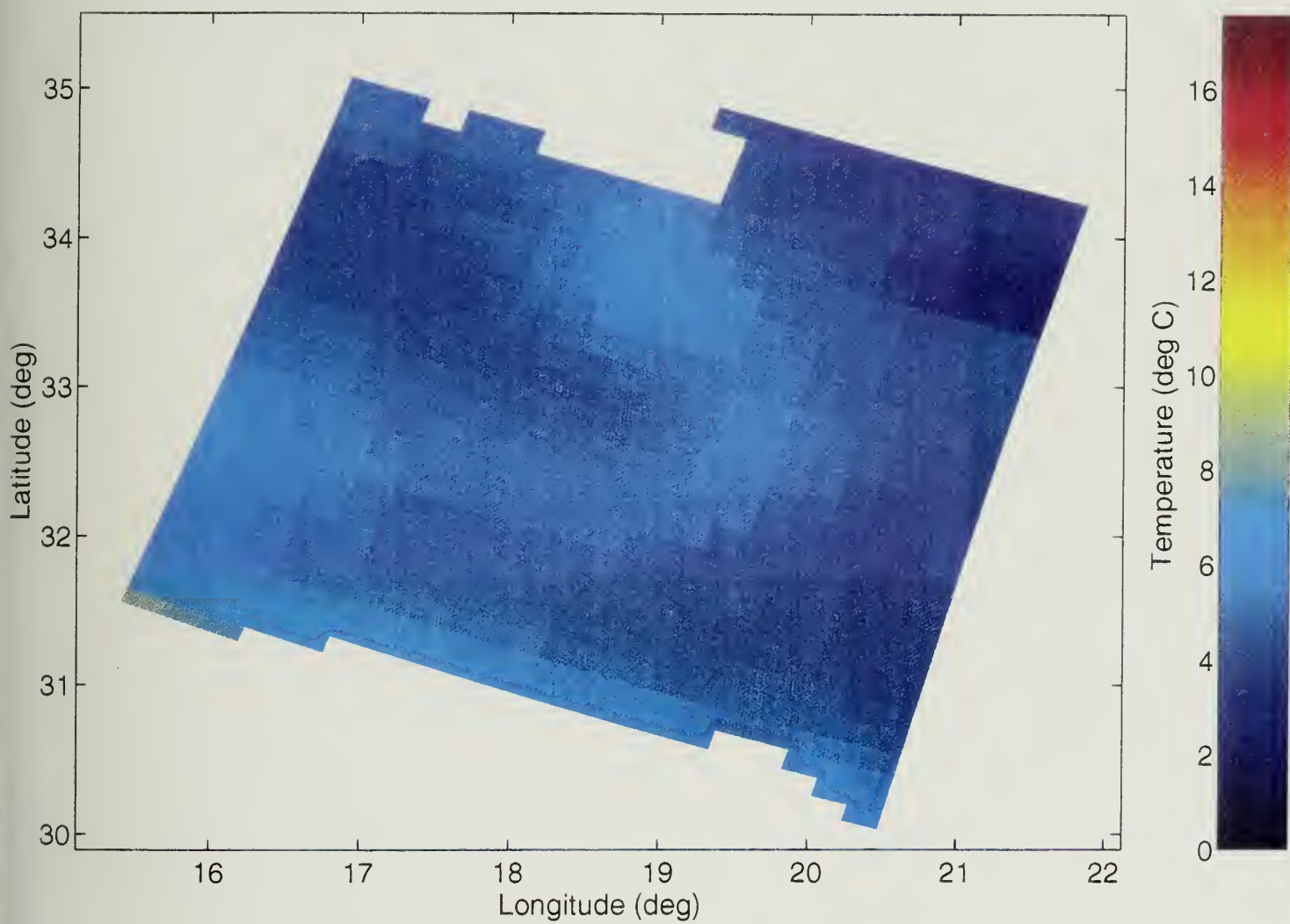


Fig. 6

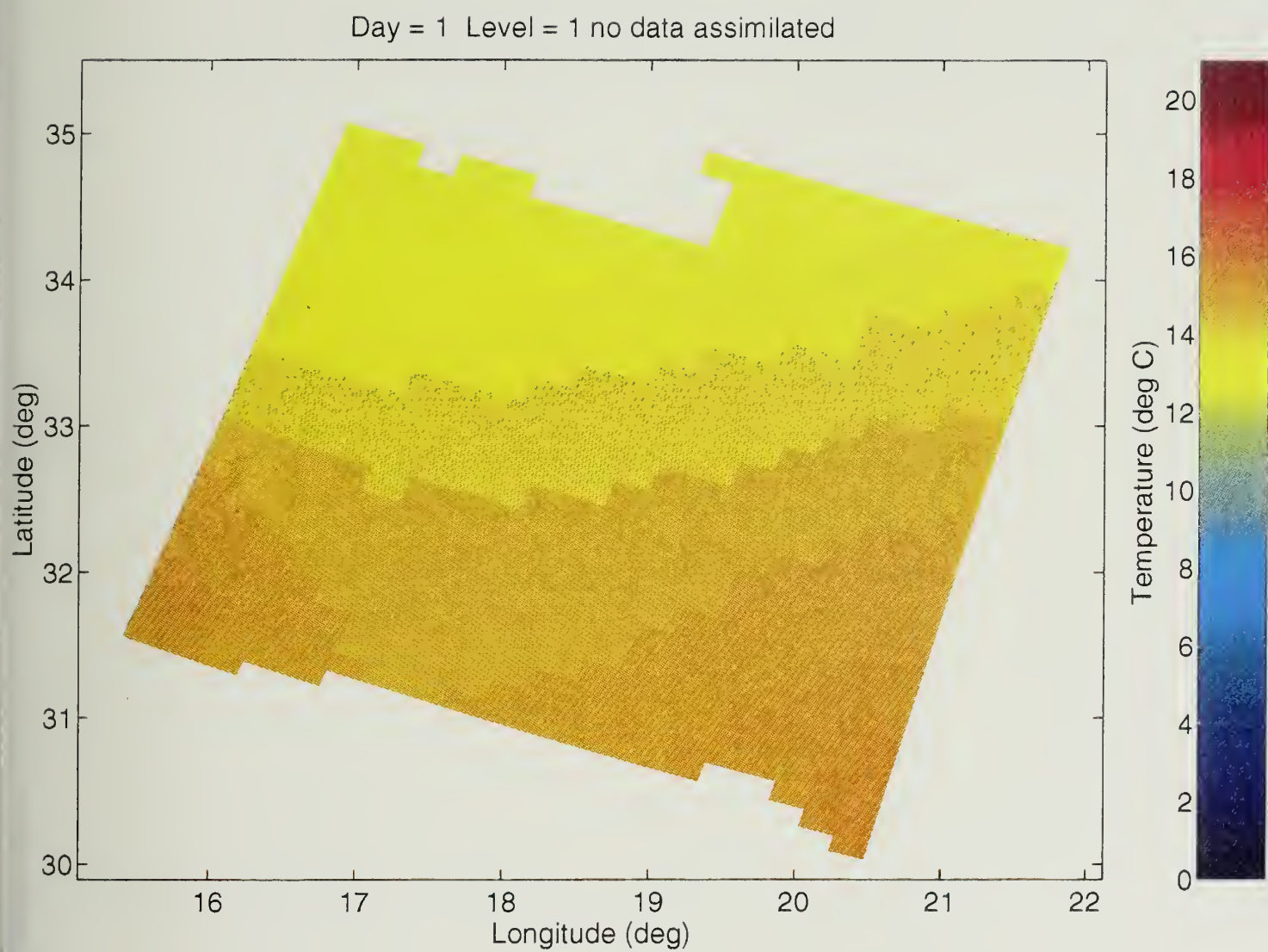


Fig. 7

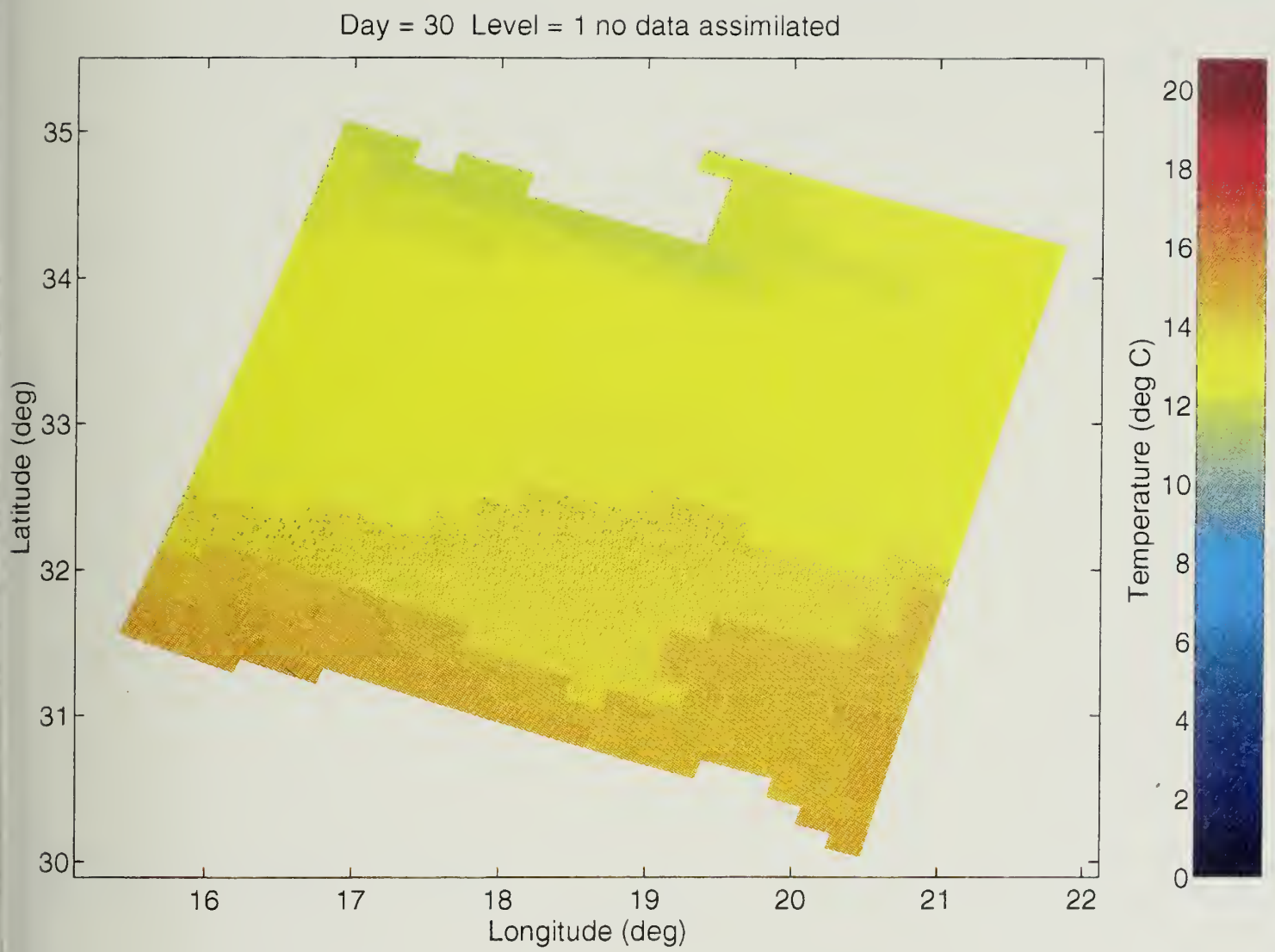


Fig. 8

No data and combined slices assimilated

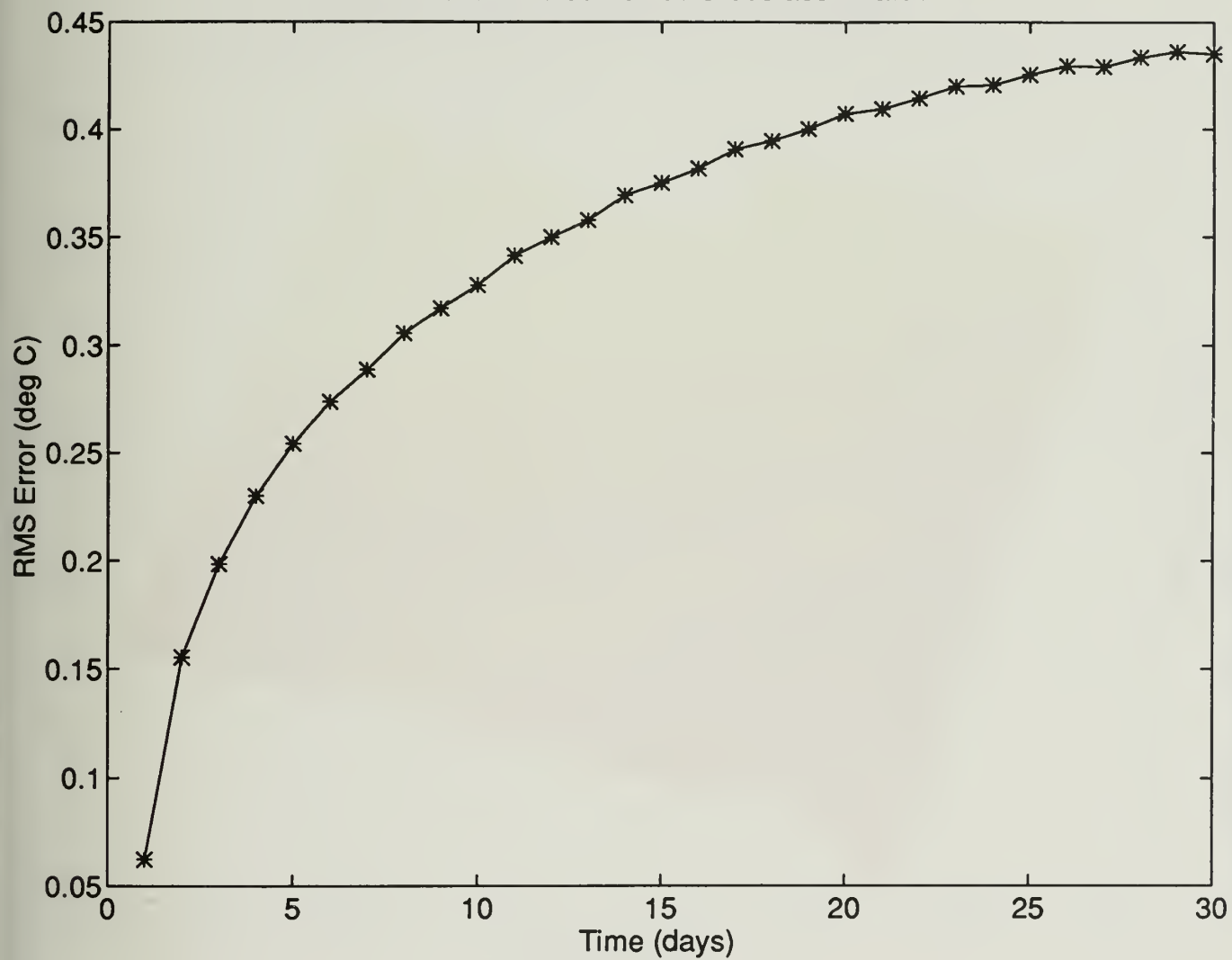


Fig. 9

Day = 1 Level = 1 NE-SW slice assimilated

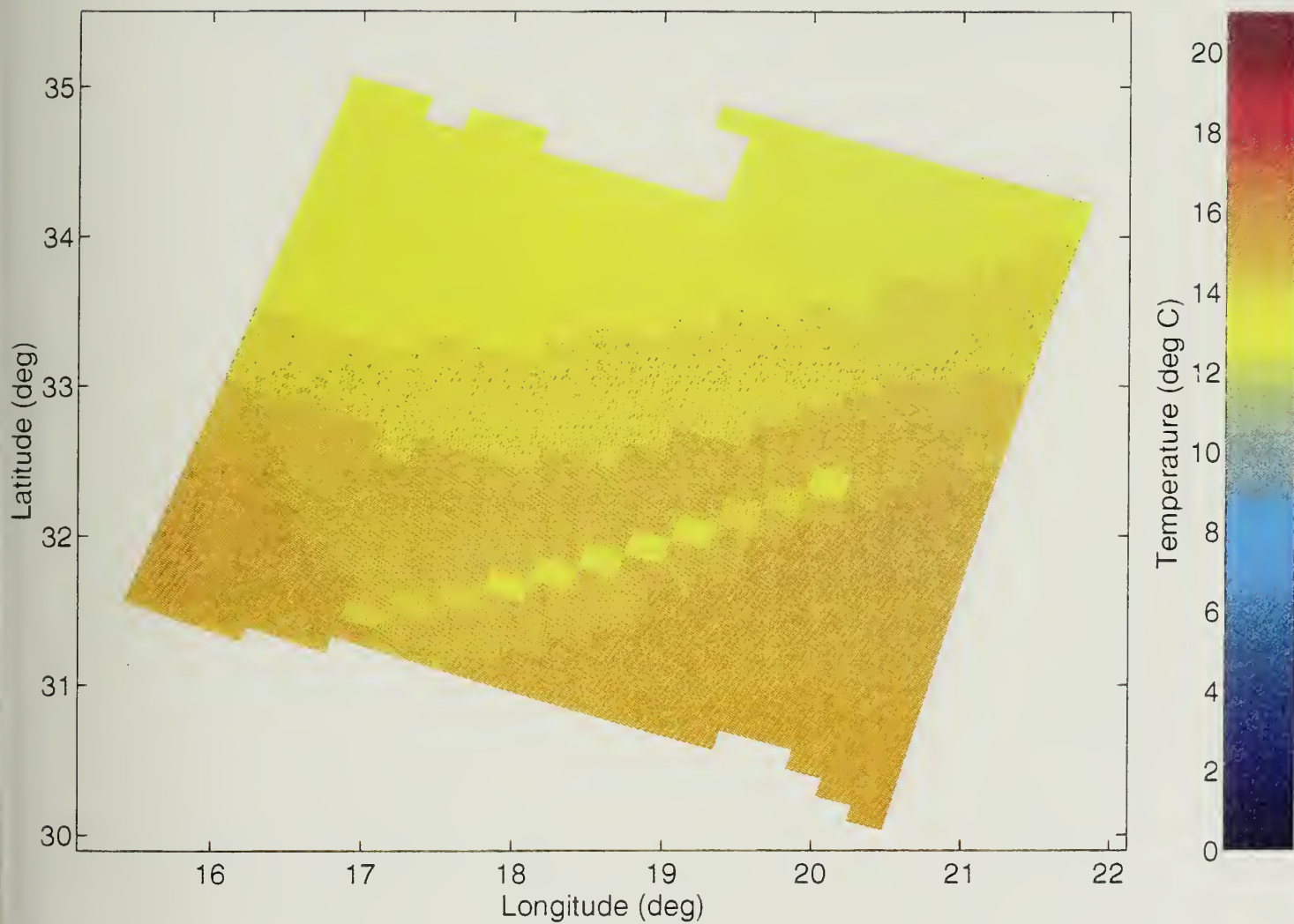


Fig. 10

Day = 1 Level = 6 NE-SW slice assimilated

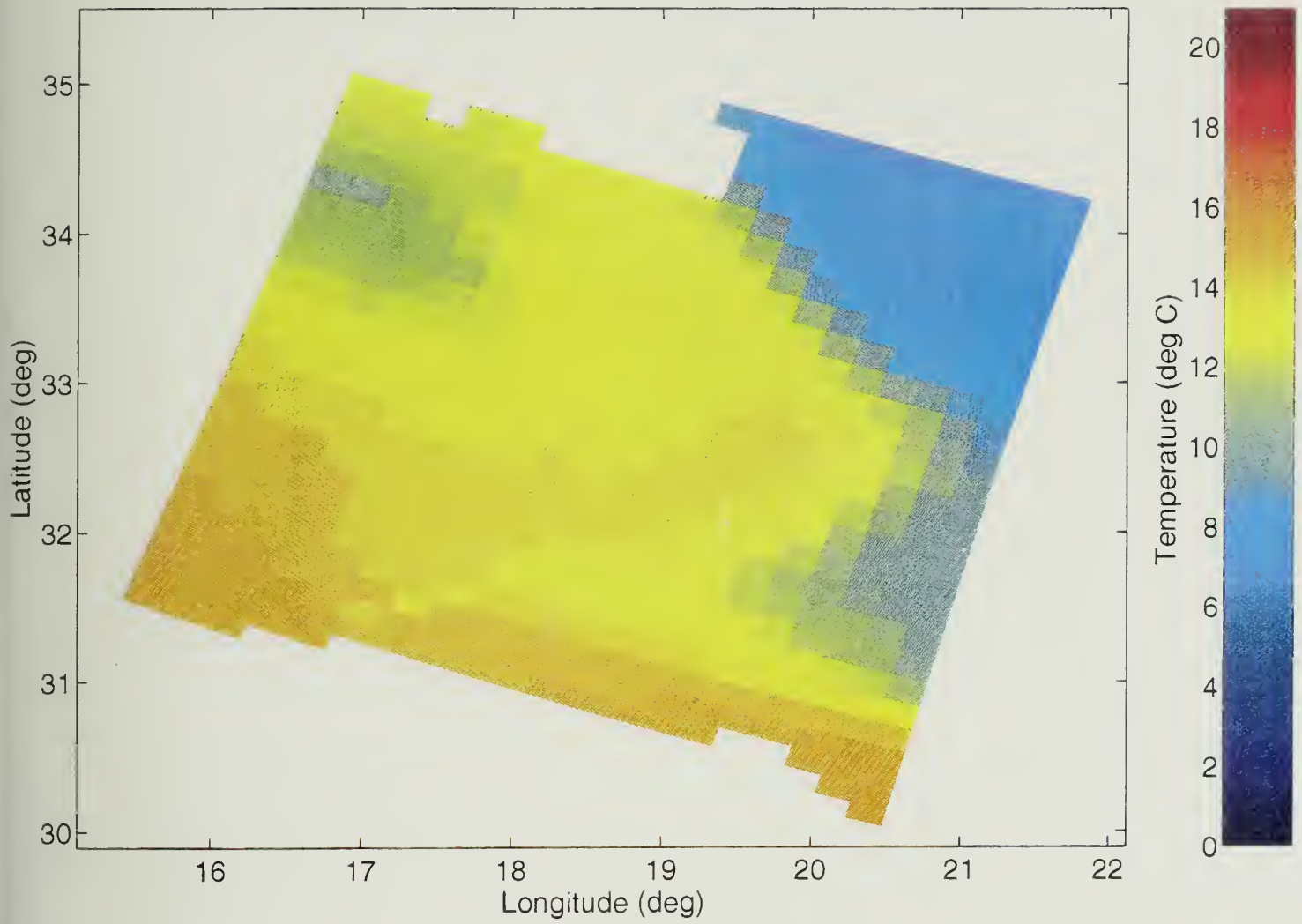


Fig. 11

Day = 1 Level = 15 NE-SW slice assimilated

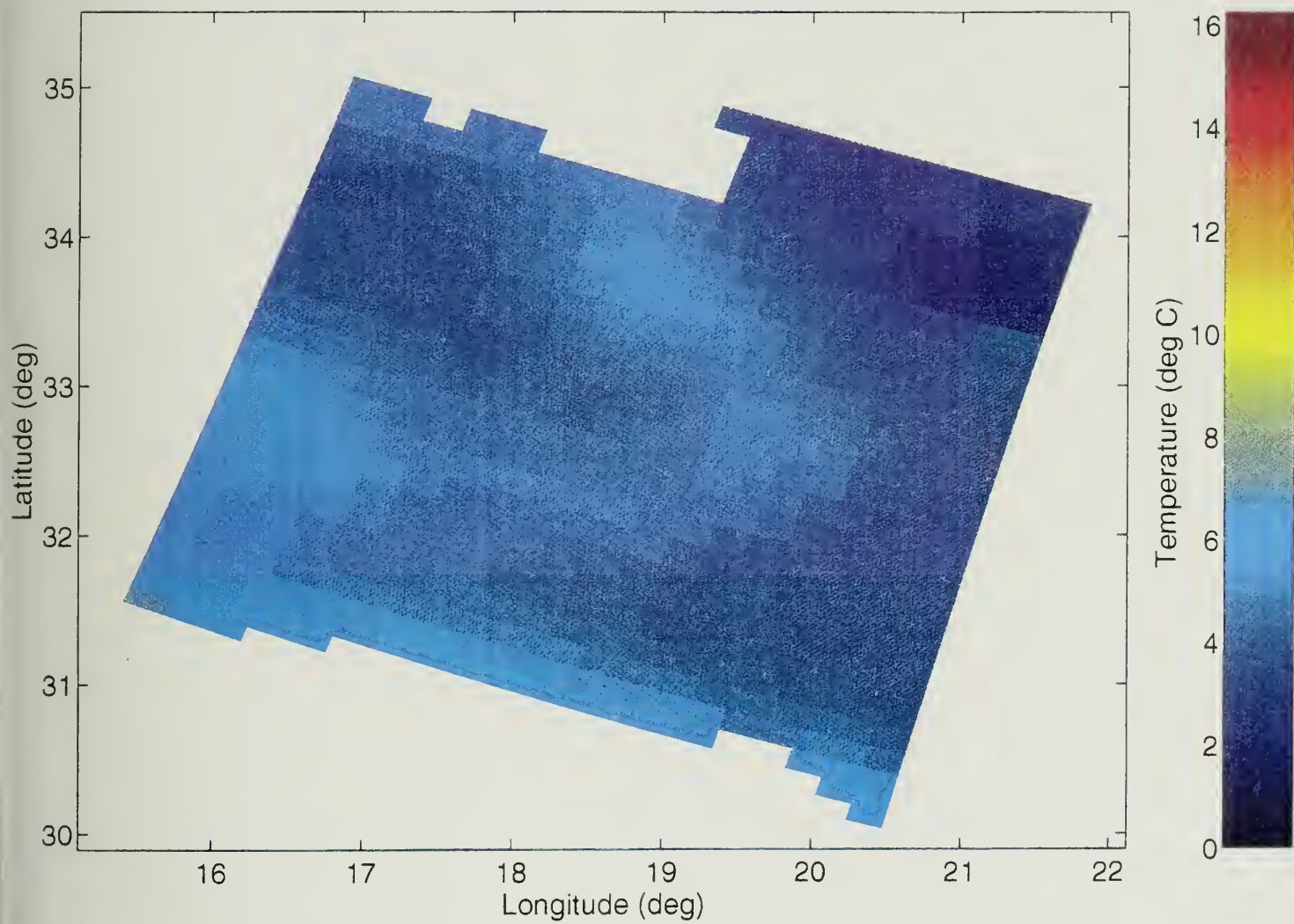


Fig. 12

Day = 30 Level = 1 NE-SW slice assimilated

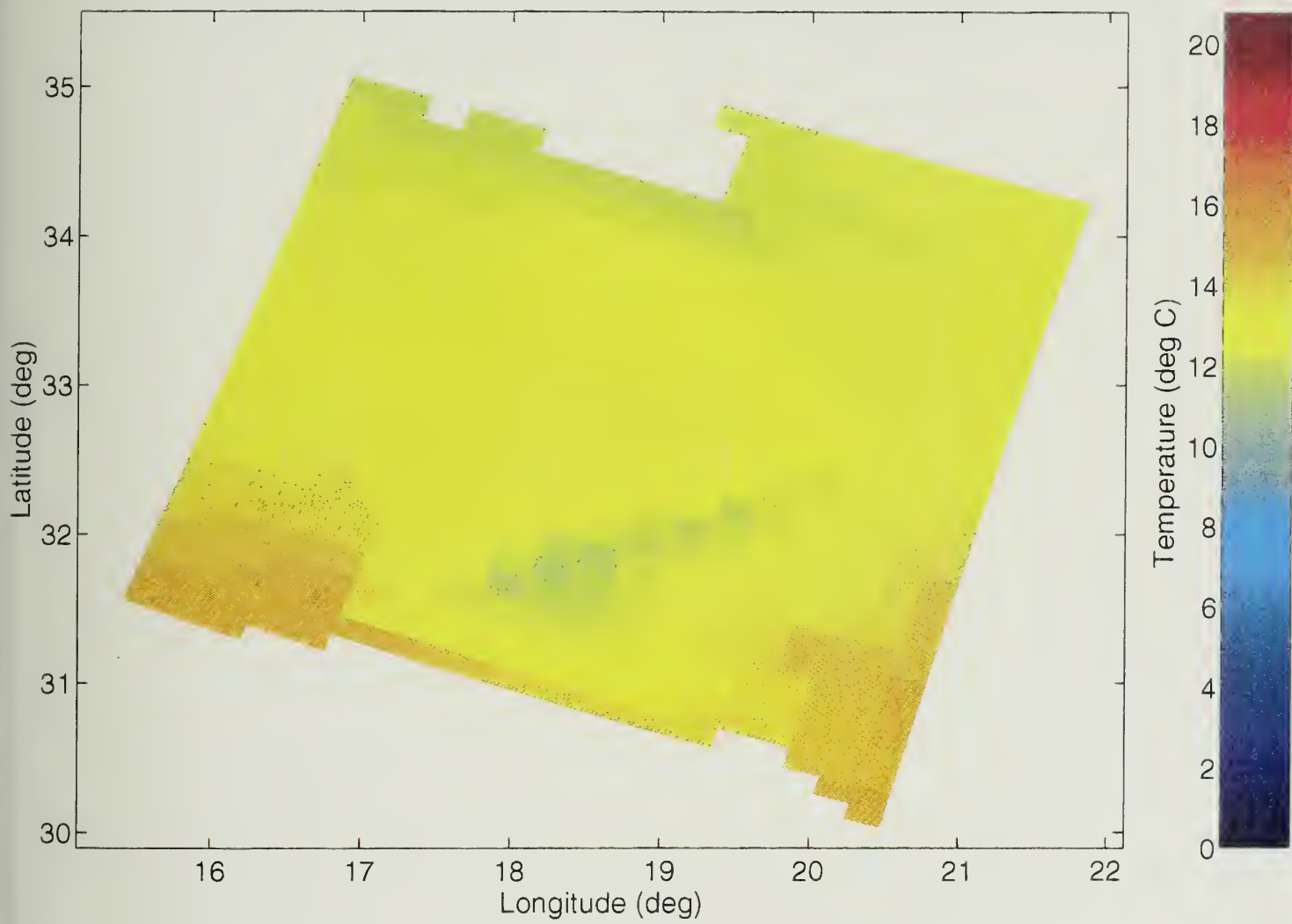


Fig. 13

Day = 30 Level = 6 NE-SW slice assimilated

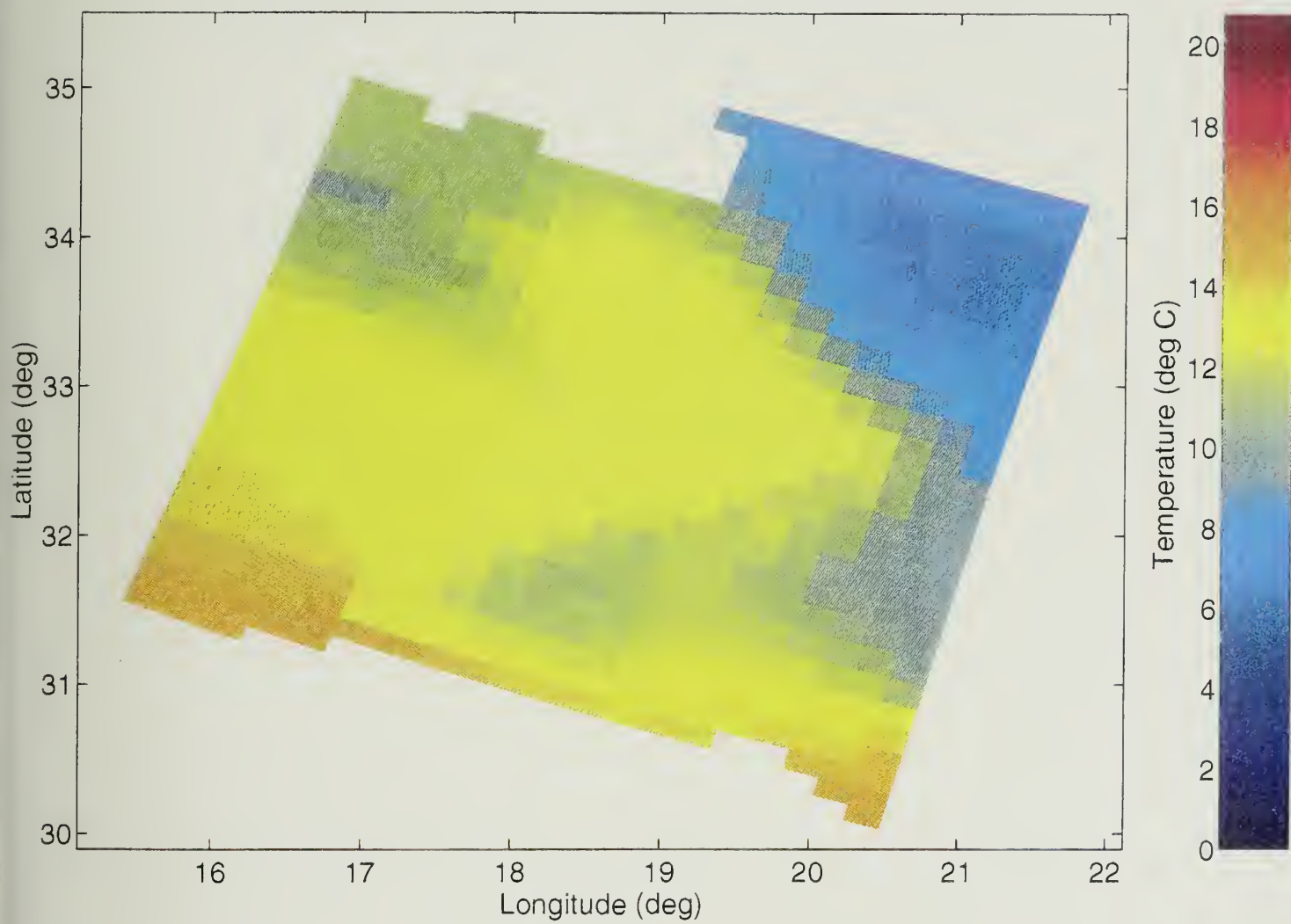


Fig. 14

Day = 30 Level = 15 NE-SW slice assimilated

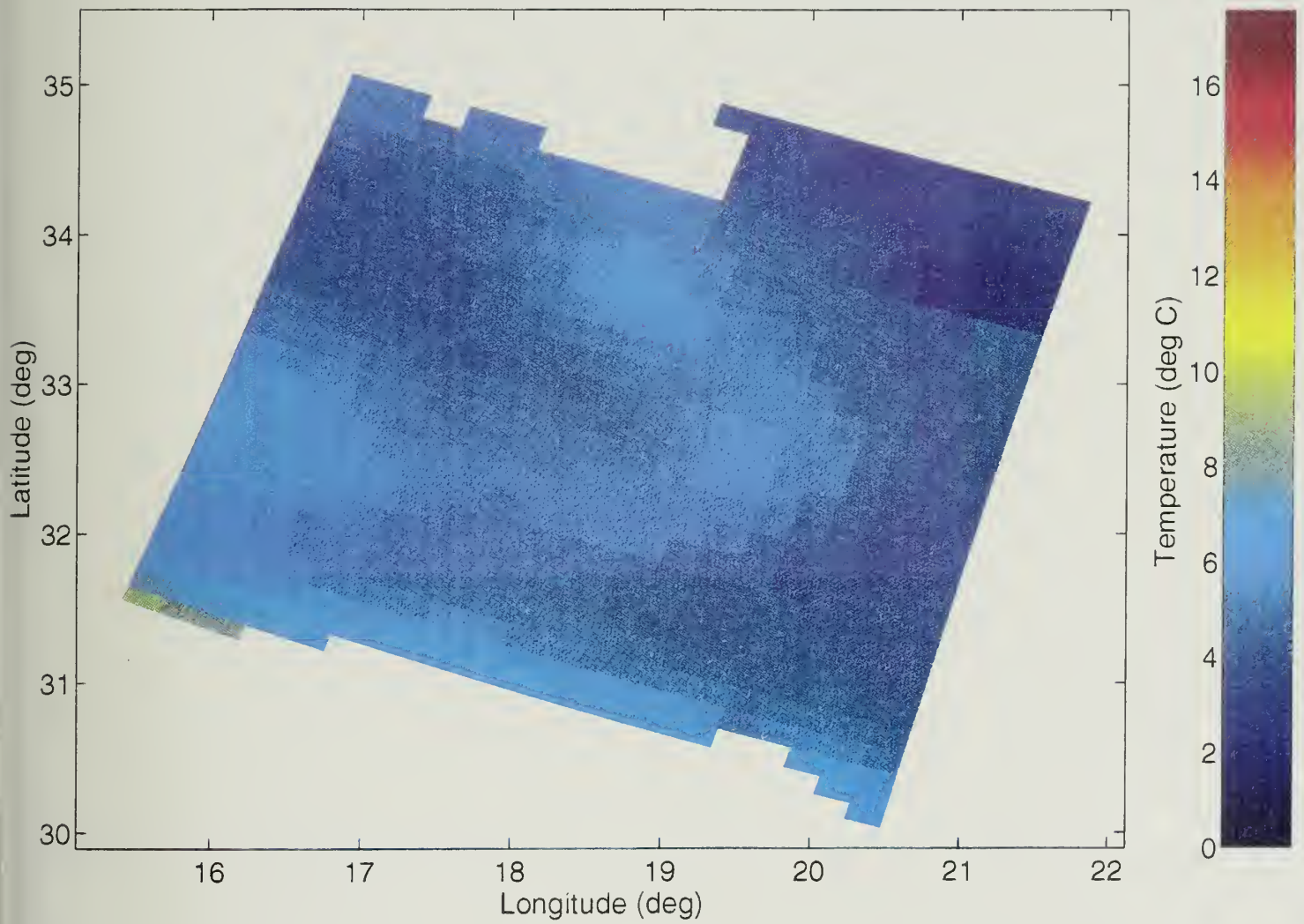


Fig. 15

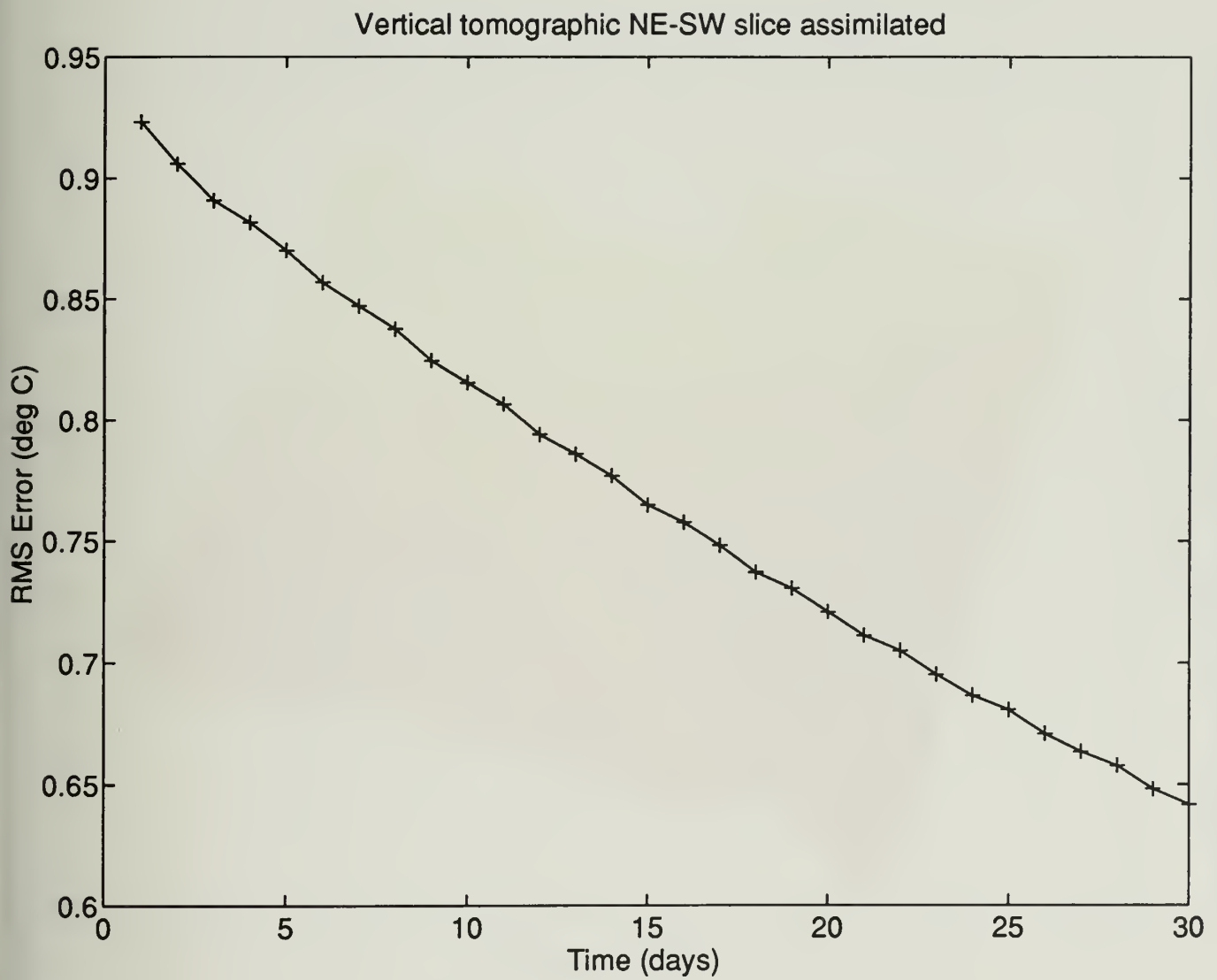


Fig. 16

Day = 1 Level = 1 NW-SE slice assimilated

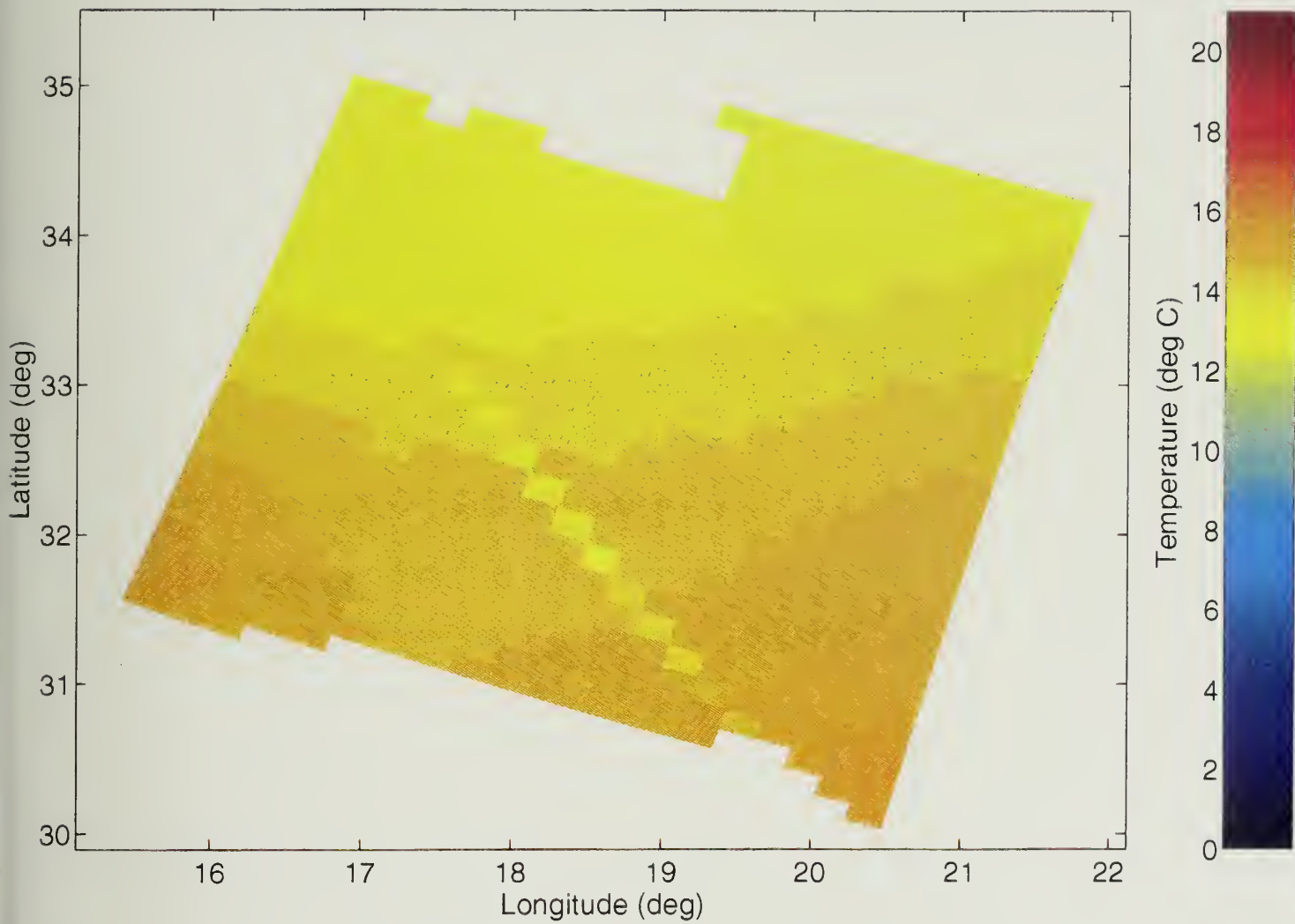


Fig. 17

Day = 1 Level = 6 NW-SE slice assimilated

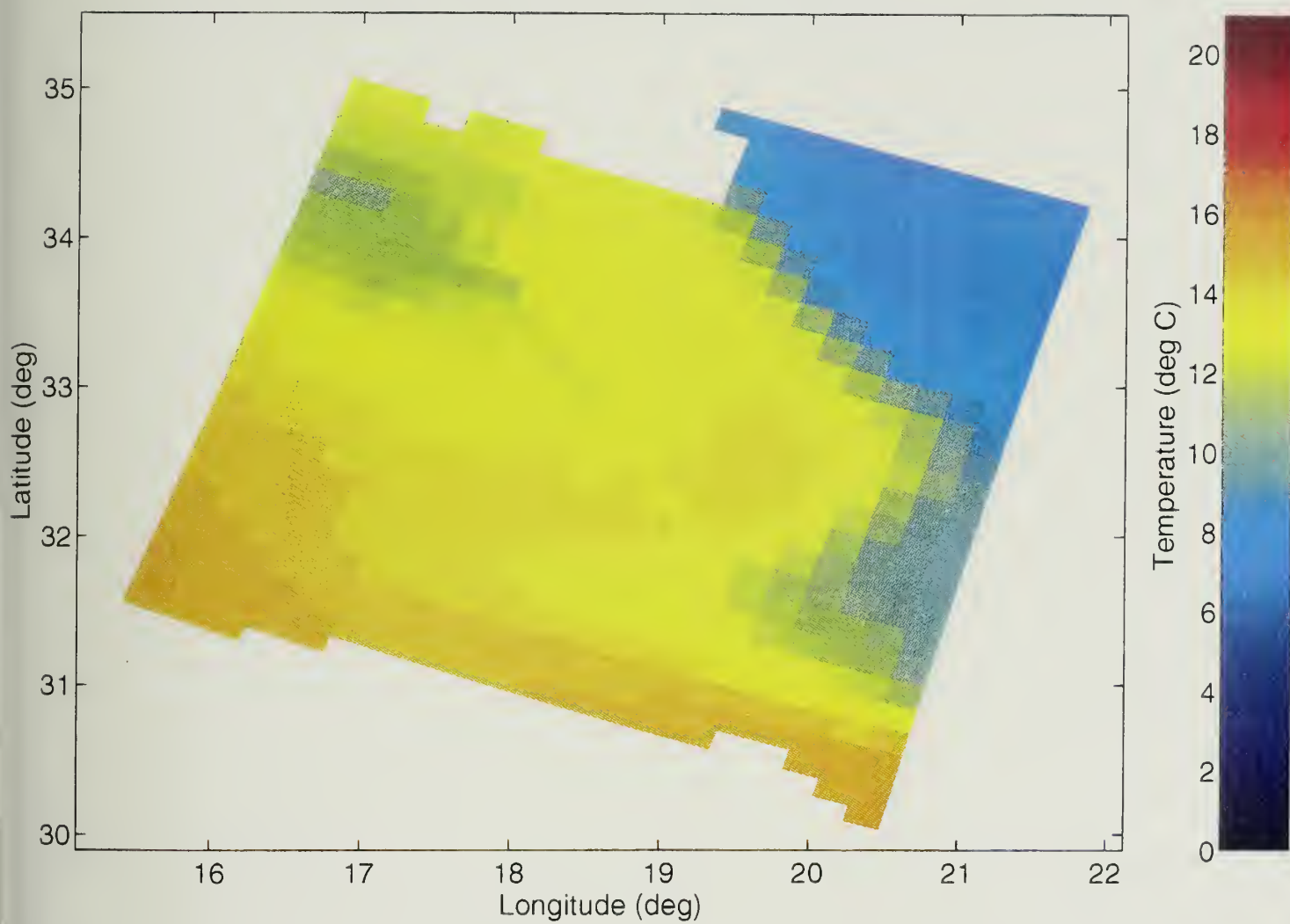


Fig. 18

Day = 1 Level = 15 NW-SE slice assimilated

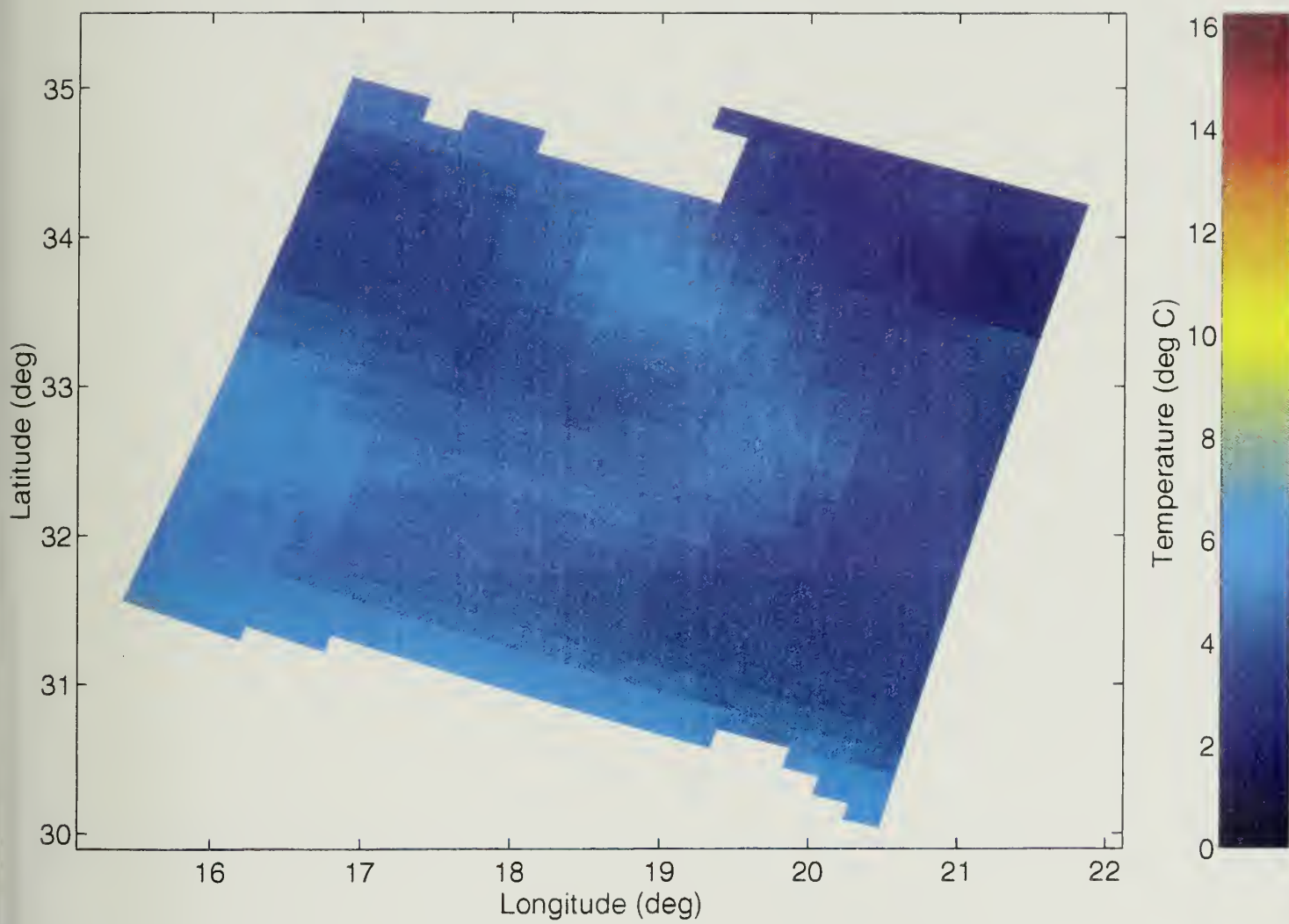


Fig. 19

Day = 30 Level = 1 NW-SE slice assimilated

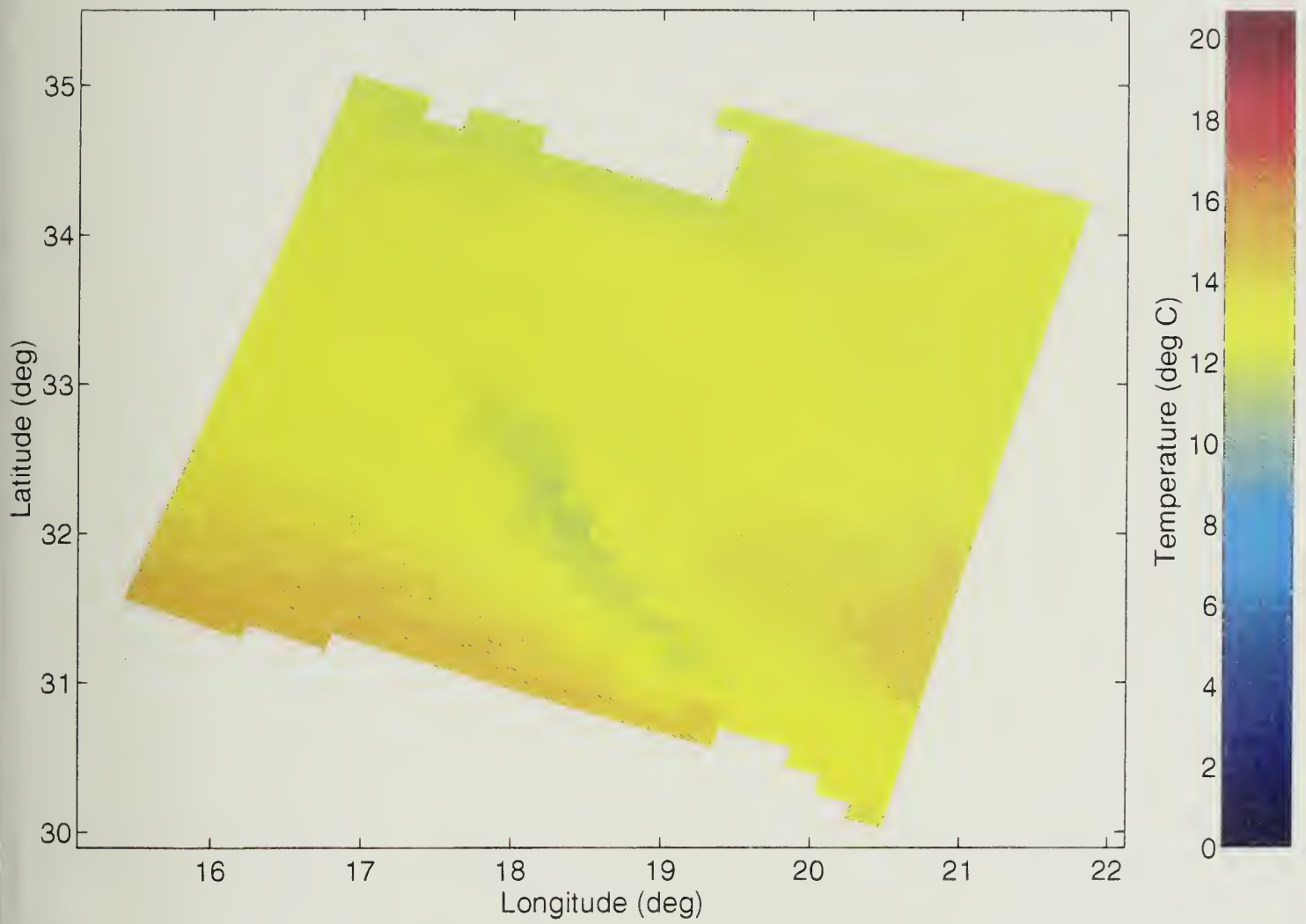


Fig. 20

Day = 30 Level = 6 NW-SE slice assimilated

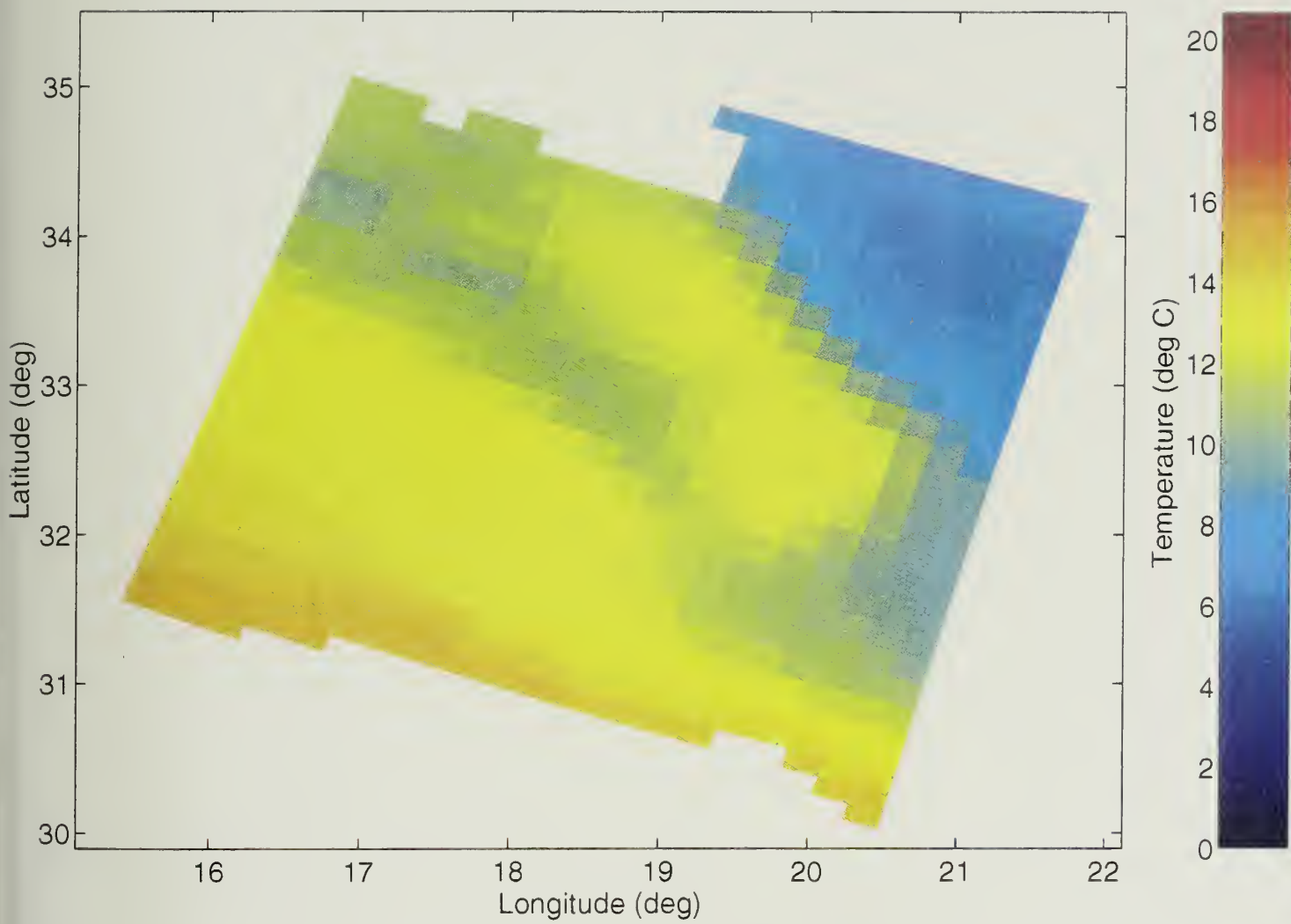


Fig. 21

Day = 30 Level = 15 NW-SE slice assimilated

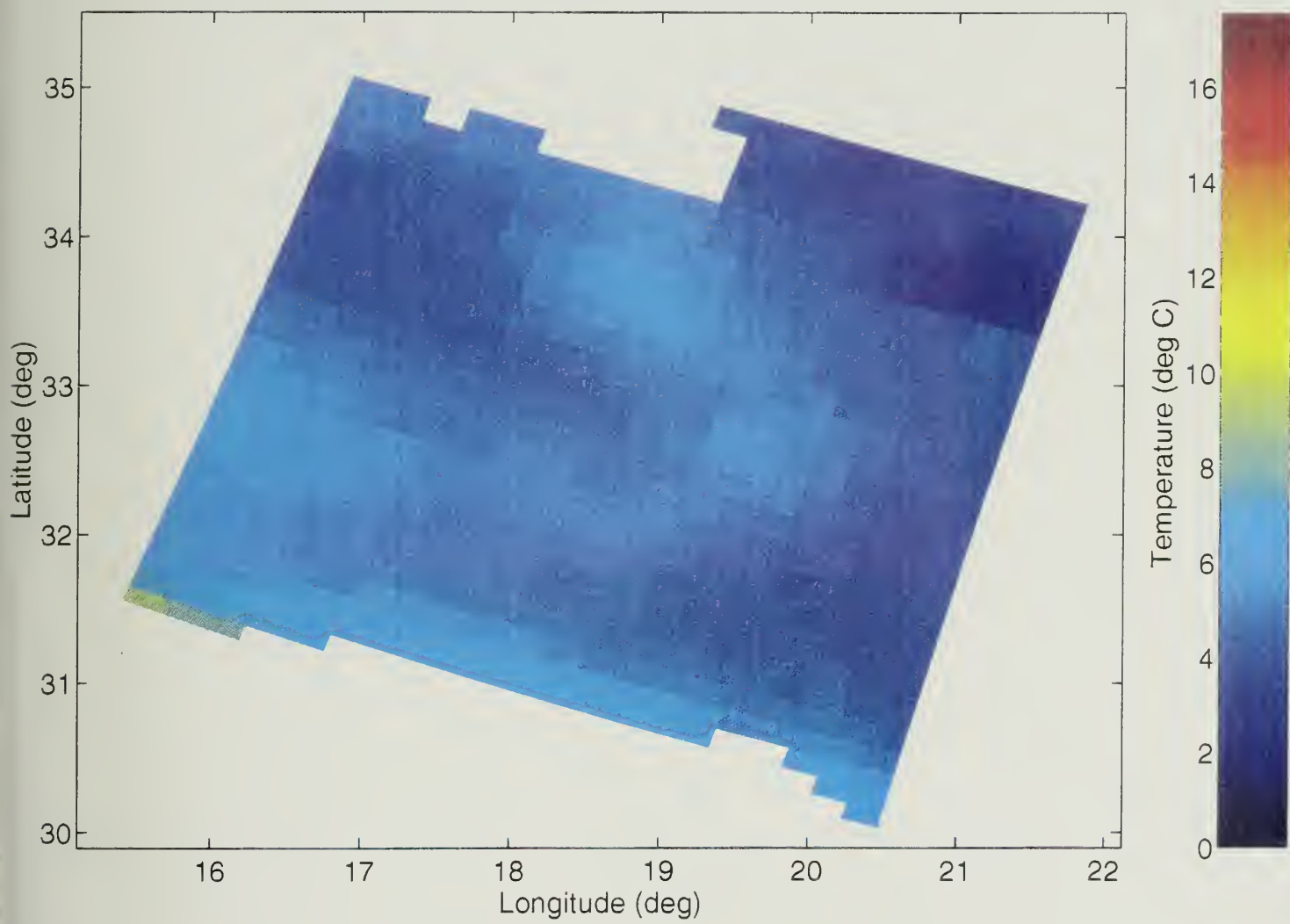


Fig. 22

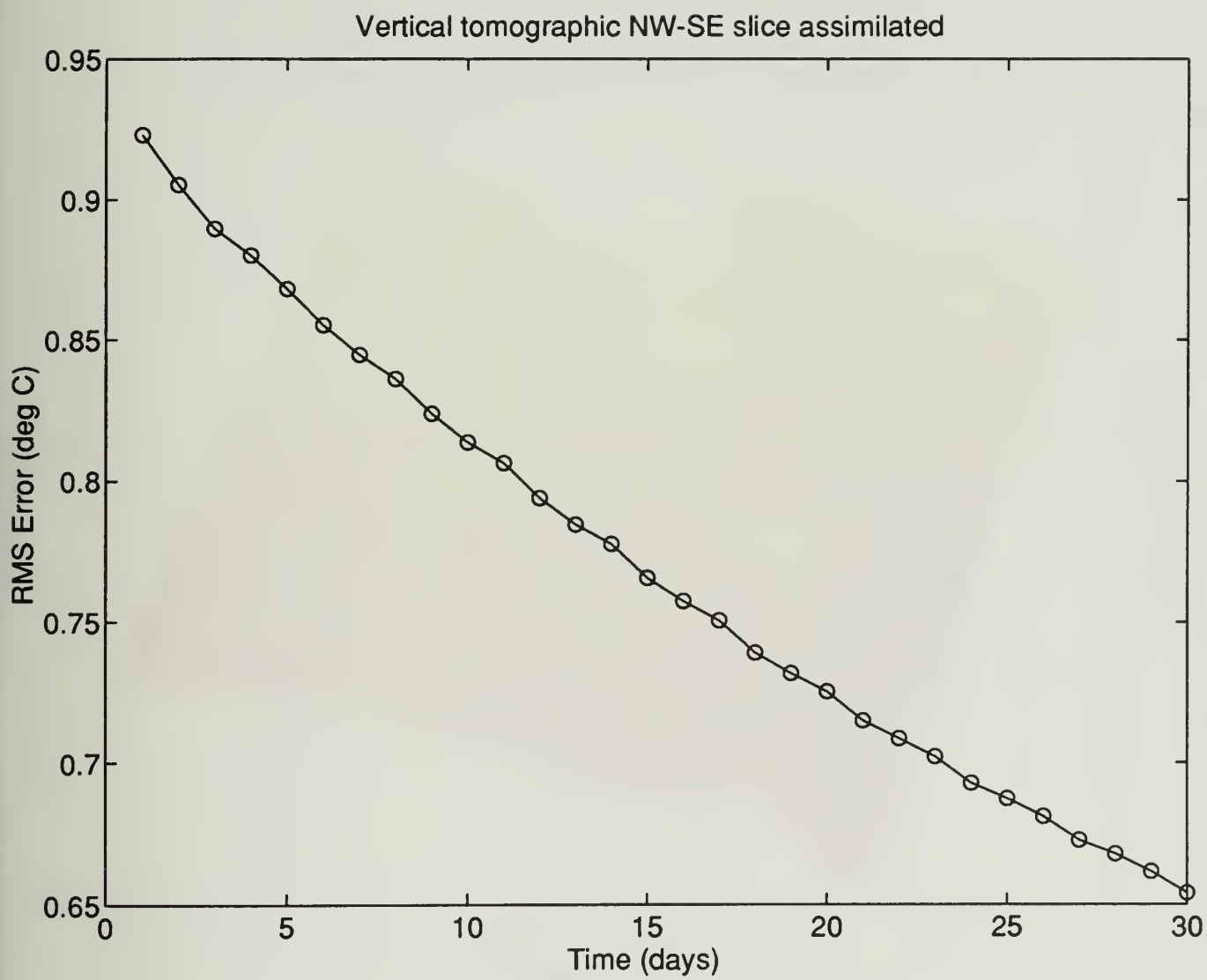


Fig. 23

Day = 1 Level = 1 Combined slices assimilated

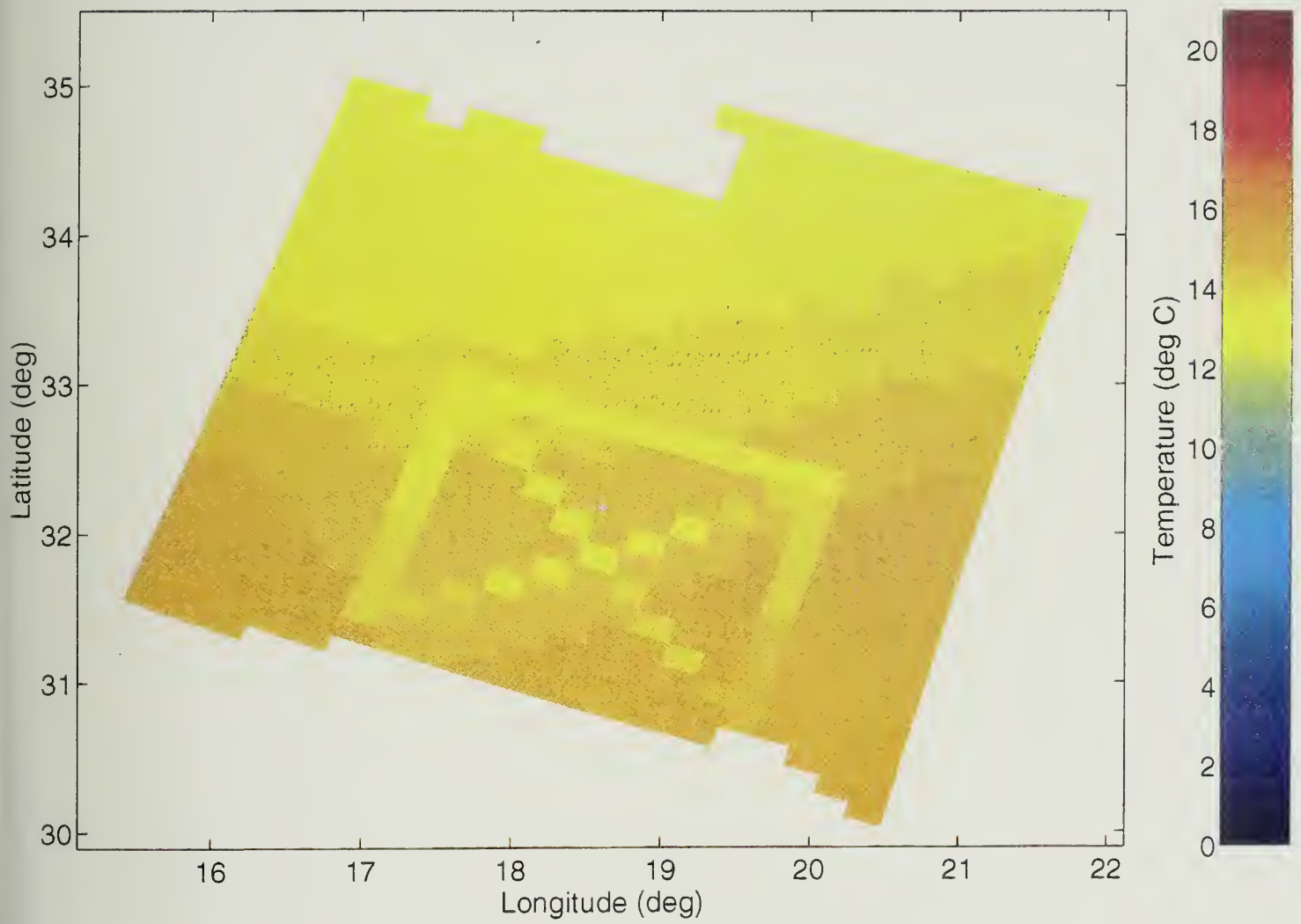


Fig. 24

Day = 1 Level = 6 Combined slices assimilated

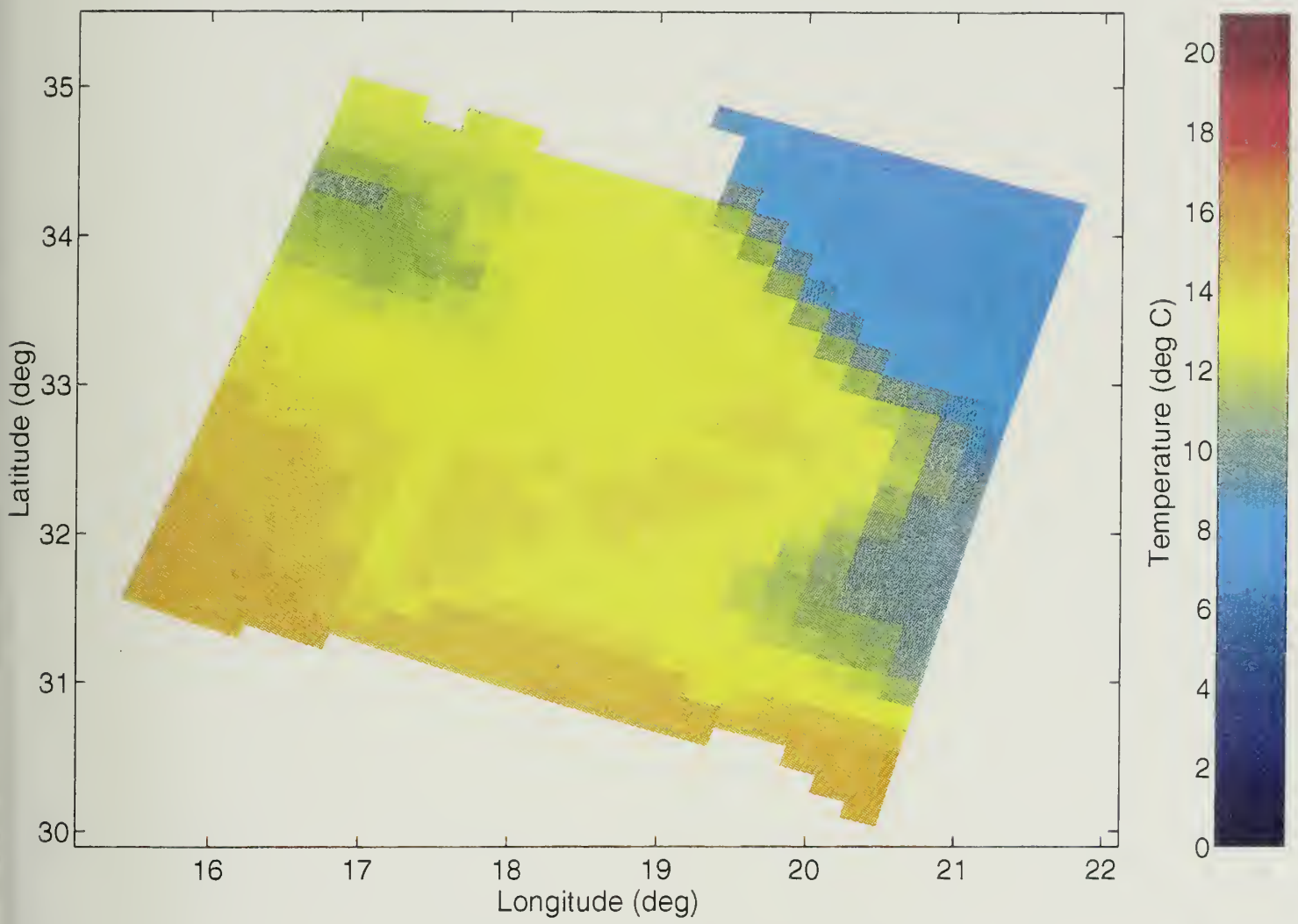


Fig. 25

Day = 1 Level = 15 Combined slices assimilated

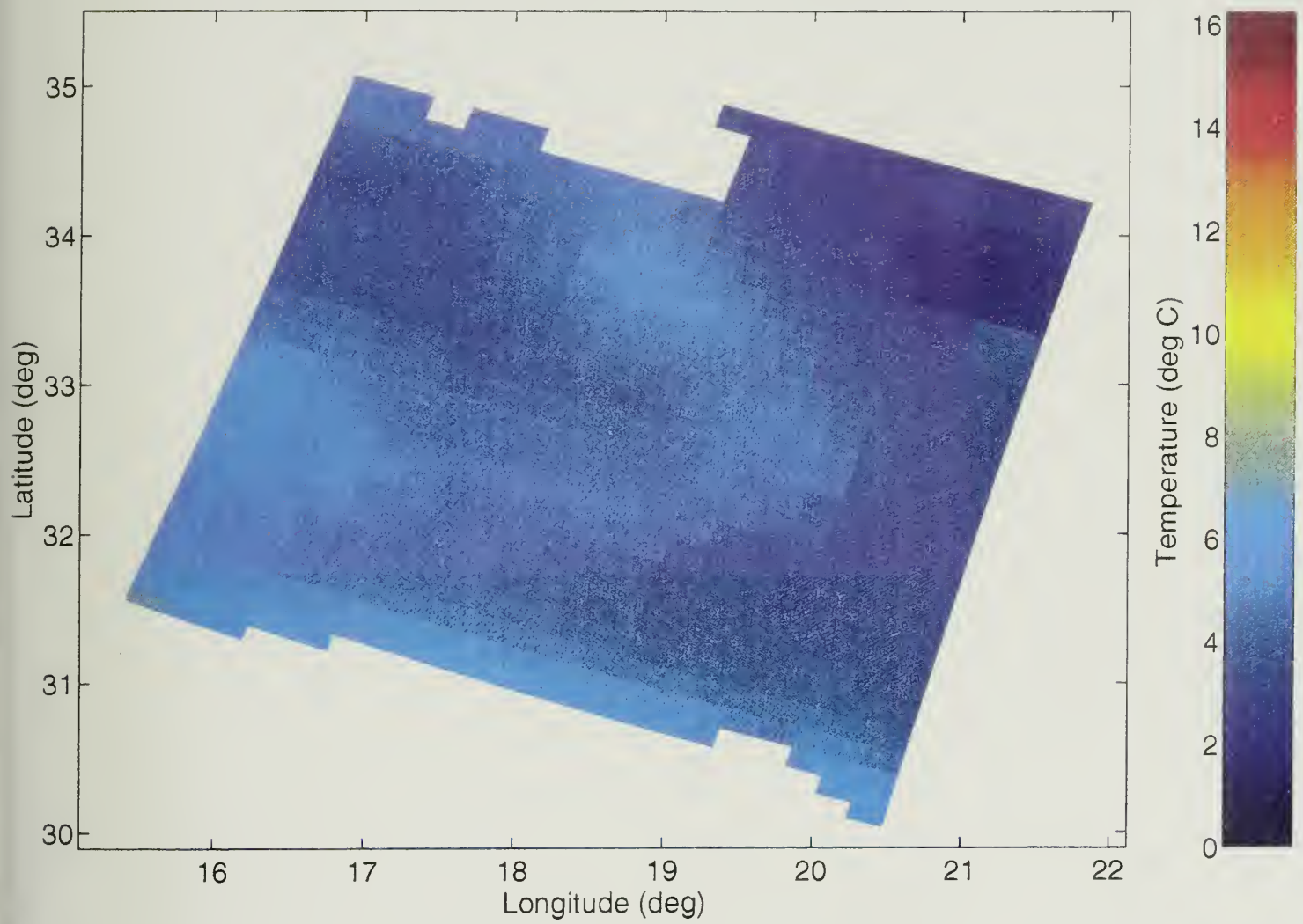


Fig. 26

Day = 30 Level = 1 Combined slices assimilated

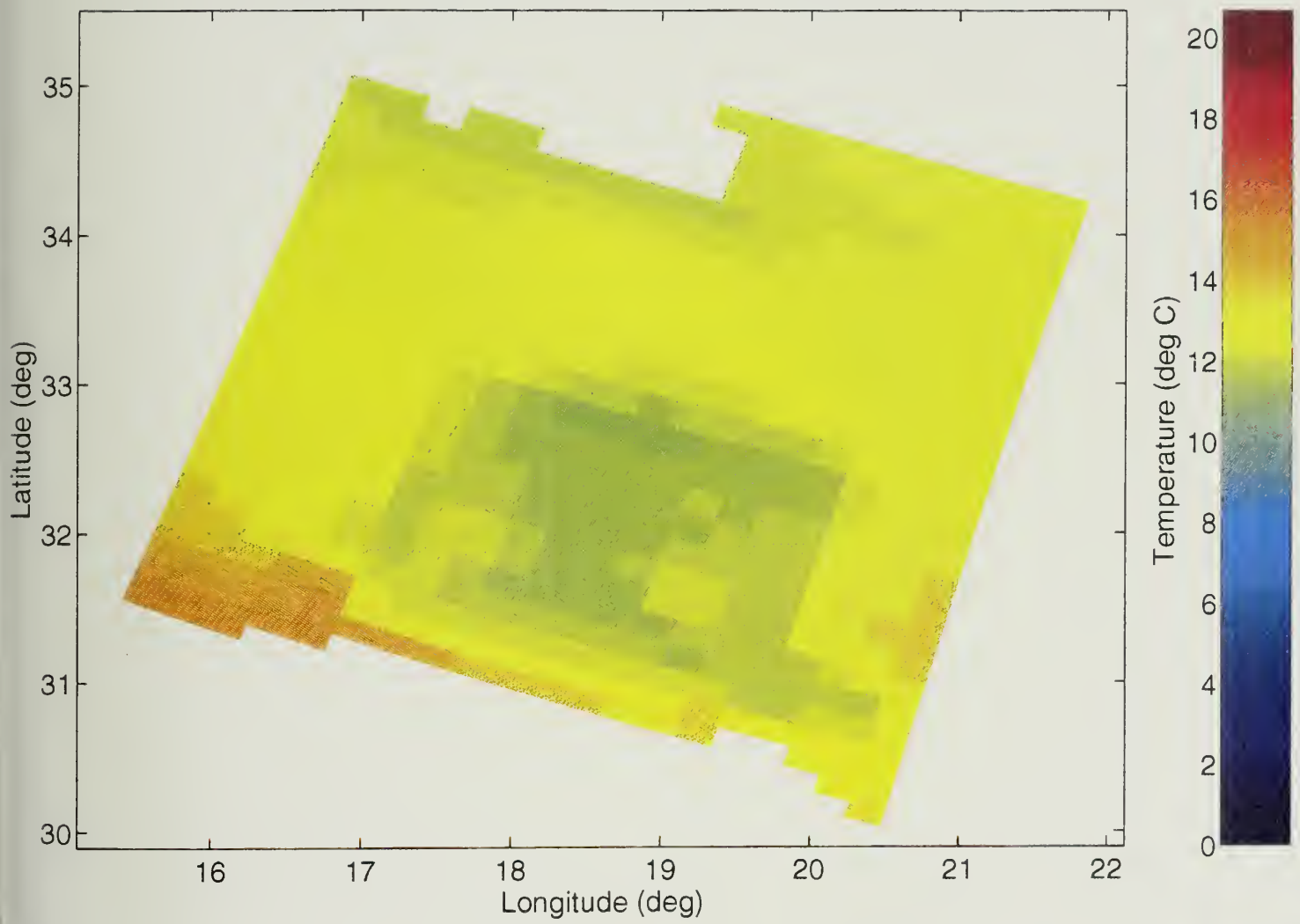


Fig. 27

Day = 30 Level = 6 Combined slices assimilated

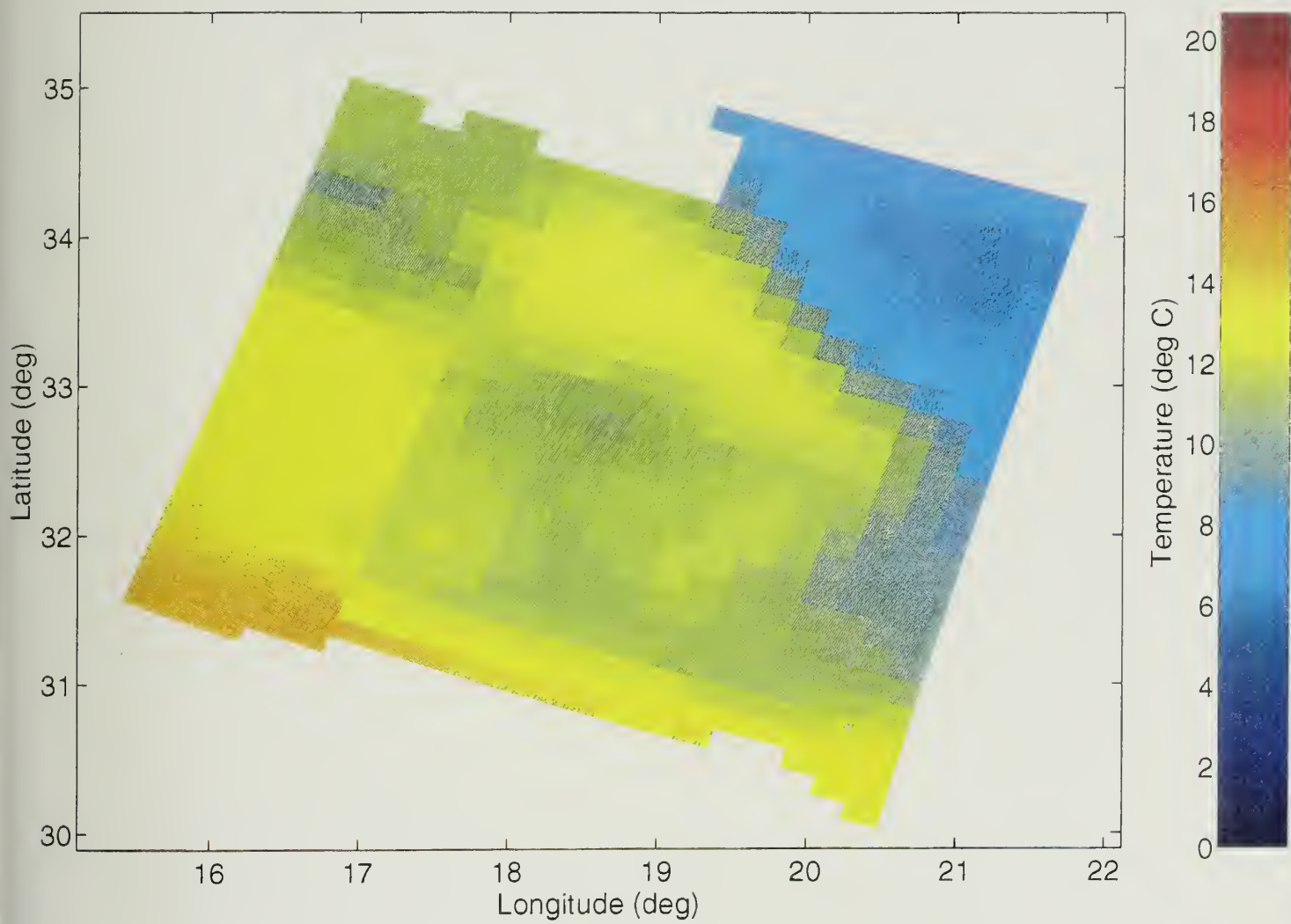


Fig. 28

Day = 30 Level = 15 Combined slices assimilated

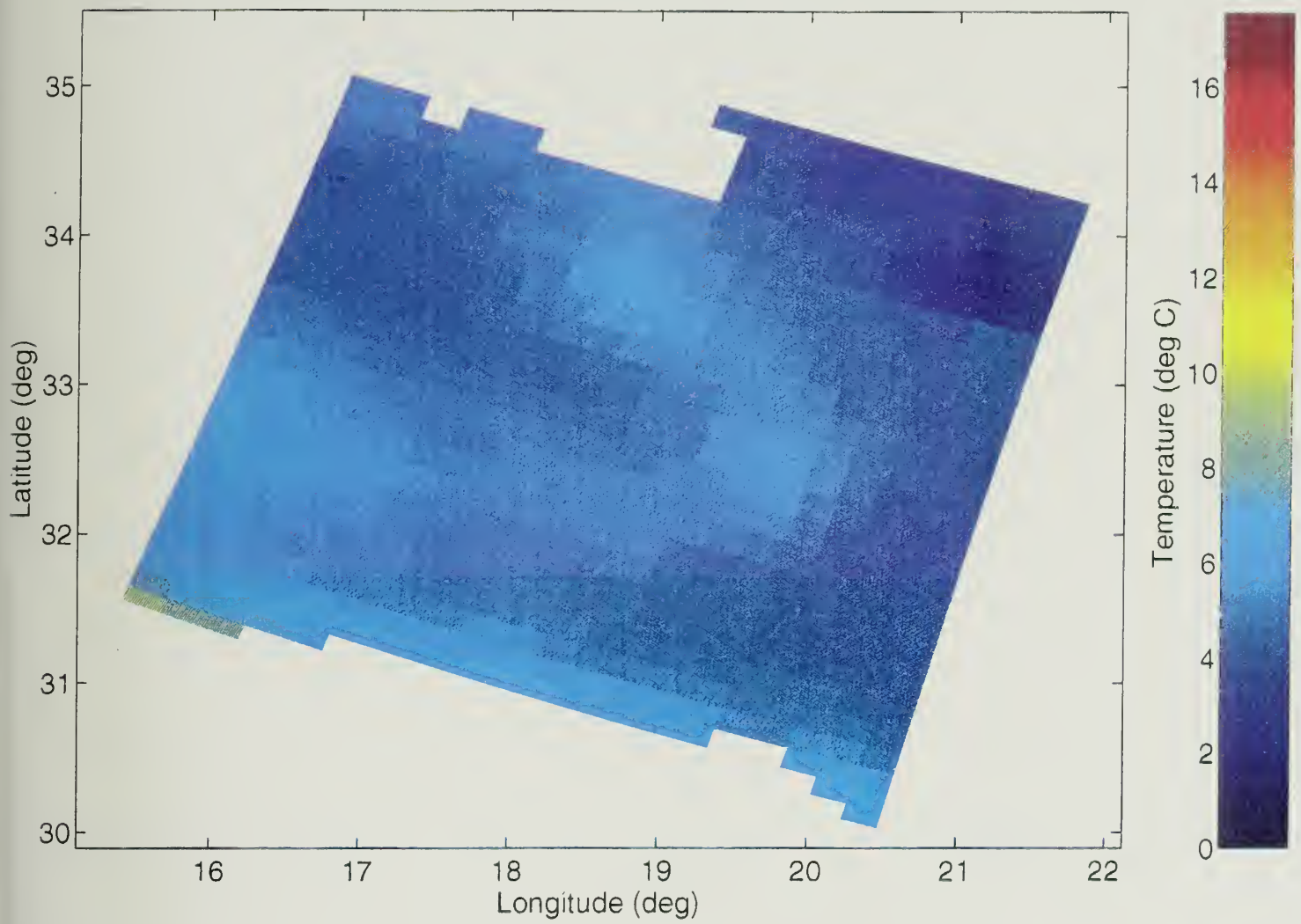


Fig. 29

Vertical tomographic combined slices assimilated

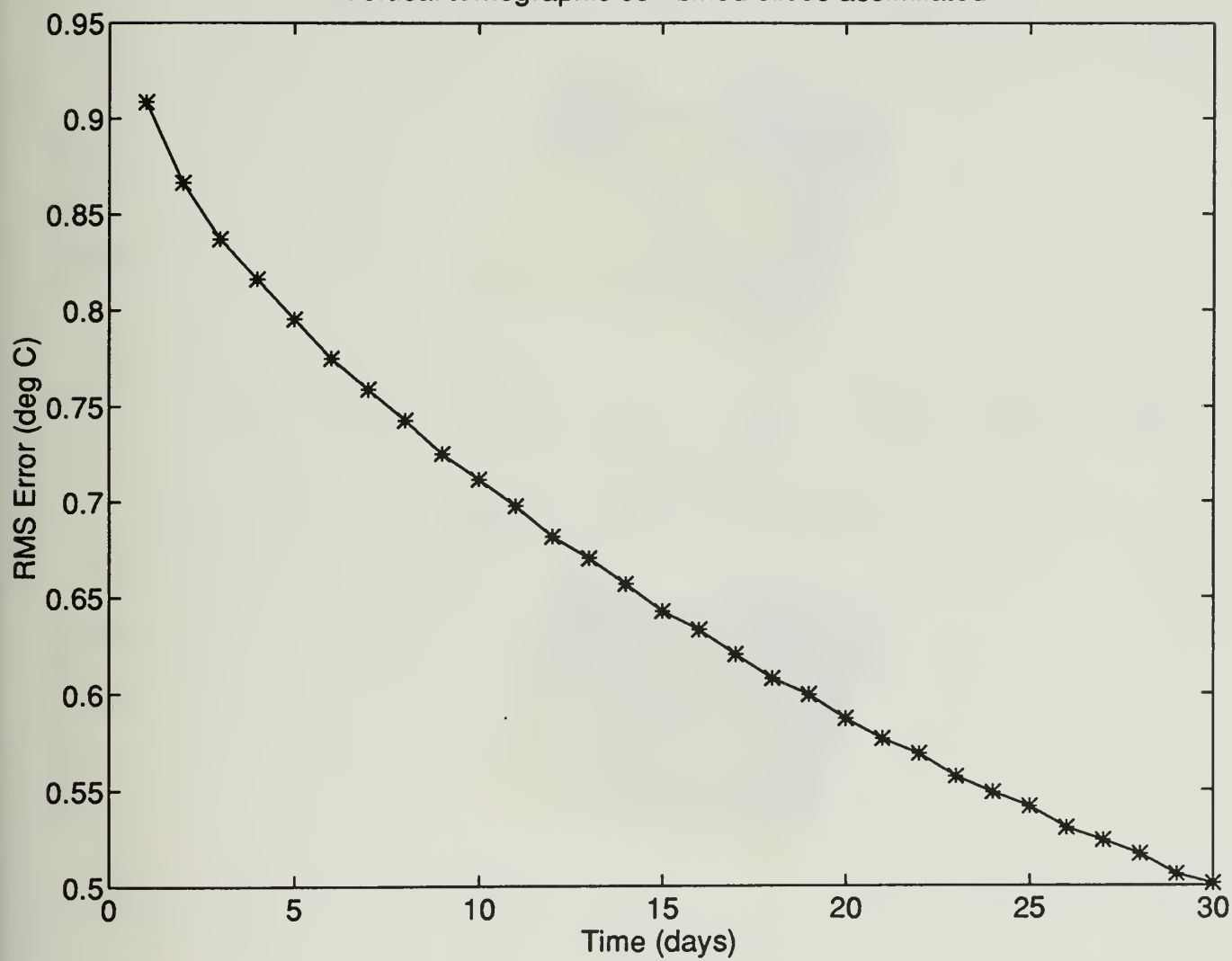


Fig. 30

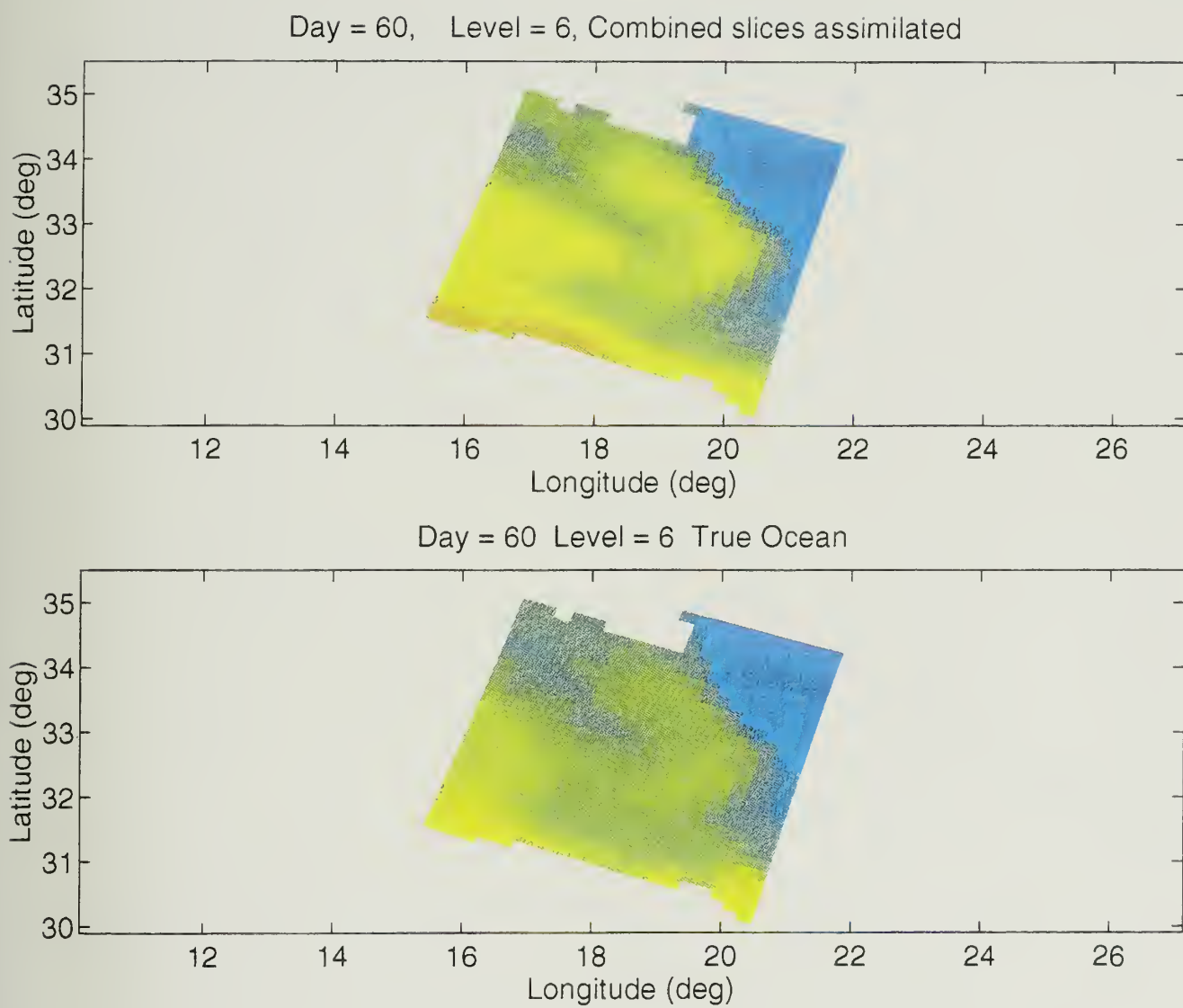


Fig. 31

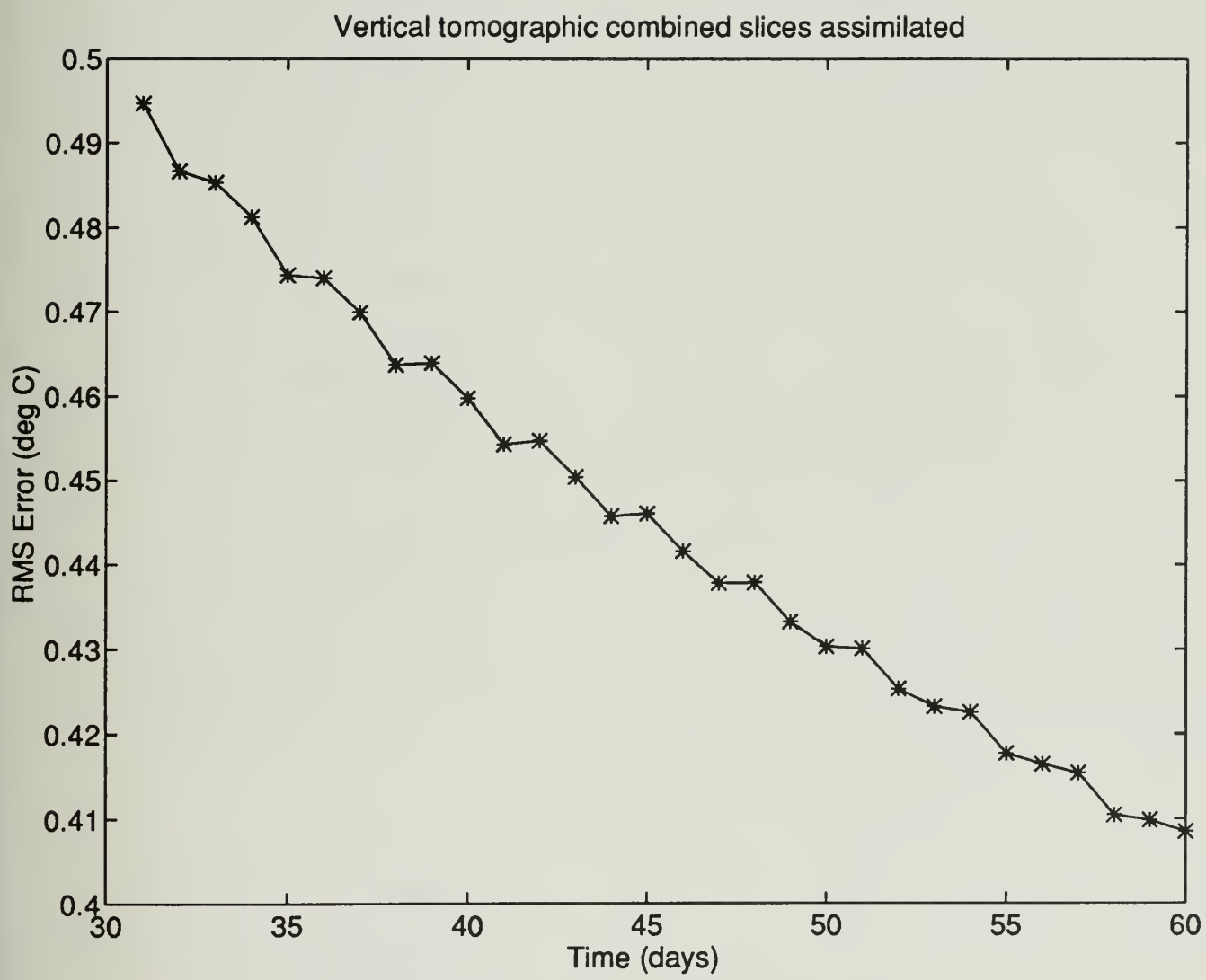


Fig. 32

INITIAL DISTRIBUTION LIST

- Office of Naval Research
800 N. Quincy Street
Arlington, VA 22217-5000
 - Dr. Arthur Bisson
 - Dr. Alan Brandt
 - Dr. Ed Chaika
 - Dr. Thomas Curtin
 - Dr. David Evans
 - Dr. Robert Feden
 - Dr. Emanuel Fiadeiro
 - Dr. Gerald Geernaert
 - Dr. Thomas Kinder
 - Dr. Mark Kurzius
 - Mr. Robert Peloquin (10)
 - Dr. Steve Ramp
 - Dr. Alan Weinstein
- National Science Foundation
4201 Wilson Blvd.
Arlington, VA 22230
 - Dr. Jay Fein
 - Dr. Eric Itswehre
 - Dr. Richard Lambert
 - Dr. Sergion Signorini
 - Dr. Silvia Garzoli
- Naval Postgraduate School
Monterey CA, 93943
 - Prof. Mary Batteen
 - Prof. Robert Bourke
 - Prof. Everett Carter
 - Prof. Curtis Collins
 - Prof. Kenneth Davidson
 - Prof. Roland Garwood

- Prof. Robert Hanney
- Libray, Code 52 (2)
- Prof. James Miller
- Office of Research
- Prof. Jeffrey Paduan
- Prof. Leslie Rosenfeld
- Prof. Albert Semtner
- Prof. Edward Thornton
- Prof. Terry Williams
- Princeton University
 - Program in the Atmospheric Oceanic Sciences
 - P.O. Box CN 710
 - Sayer Hall, Princeton, NJ 08544-0710
 - Prof. George Mellor
 - Dr. Tal Ezer
- Defense Technical Information Center (2)
 - Cameron Station
 - Alexandria, VA 22304-6145
- Naval Oceanographic Office
 - 1002 Balch Blvd
 - Stennis Space Center, MS 39522-5001
 - Dr. Don Durham
 - Mr. Steve Haeger
 - Dr. Martha Head
 - Dr. Charles Horton
 - Mr. Andrew Johnson
 - Dr. Phu Luong
- Fleet Numerical Oceanography Center
 - 7 Grace Hopper Ave. Stop 1
 - Monterey CA, 93943-5501
 - Dr. Mike Clancy
 - Dr. Jim Cummings
 - Cap. Robert Plante

- Naval Research Laboratory
7 Grace Hopper Ave. Stop 2
Monterey, CA 93943-5006
 - Dr. Edward Barker
 - Dr. Simon Chang
 - Dr. John Glendenning
 - Dr. Jim Goerss
 - Dr. Richard Hodur
 - Dr. John Hovermale
 - Dr. Tom Rosmond
 - Dr. Patricia Phoebus
- Naval Research Laboratory
Stennis Space Center, MS 39529
 - Dr. Patrick Gallacher
 - Dr. Abert Green, Jr.
 - Dr. John Harding
 - Dr. George Heburn
 - Dr. Harley Hurburt
 - Dr. Edward Johnson
 - Dr. John Kindle
 - Dr. Paul Martin
 - Dr. William Mosely
 - Dr. Steve Piacsek
 - Dr. Ruth Prellor
 - Dr. Kim Suanders
- National Center for Atmospheric Research
P.O. Box 3000, Boulder, CO 80307-3000
 - Dr. Richard A. Anthes
 - Dr. William Holland
- National Meteorological Center
5200 Auth Road
Washington, D.C. 20233
 - Dr. Ron McPherson
 - Prof. Lev Gandin

- Prof. Dmitry Chalikov
- National Ocean Service
Estuarine and Ocean Physics Branch
6010 Executive Blvd.
Rockville, MD 20852
 - Dr. Wayne Wilmot
 - Dr. Henry Frey
- Florida State University
Tallahassee, FL 32306
 - Prof. James O'Brien
Mesoscale Air-Sea Interaction Group
Dept. of Meteorology
 - Supercomputer Computations Research Institute
 - Dept. of Oceanography
- Woods Hole Oceanographic Institute
Woods Hole, MA 02543
 - Dr. Ken Brink
 - Dr. Dave Chapman
 - Dr. Hsiao-Ming Hsu
 - Dr. William Schmitz
- Harvard University
Center for Earth and Planetary Physics
29 Oxford Street, Room 100D
Cambridge, MA 02138
 - Prof. Allan Robinson
 - Dr. Mohsen Pourkaviani
- Massachusetts Institute Technology
Dept. of Earth, Atmospheric and Planetary Science
Cambridge, MA 02139
 - Prof. Paola Rizzoli
 - Prof. Carl Wunsch
- NASA Goddard Space Flight Center
Greenbelt, MD 20771
 - Dr. Tony Busalacchi

- Dr. Michele Rienecker
 - Dr. Fox Rabinovitz
 - Dr. R. L. Bates
- Oregon State University
Corvallis, OR 97331-2849
 - Dr. John Allen
 - Dr. Andrew Bennett
- University of Miami
4600 Rickenbacker Causeway
Miami, FL 33149-1098
 - Div. of Meteorology and Physical Oceanography
 - Dr. Christopher Mooers
- Scripps Institute of Oceanography
LaJolla, CA 92093
 - Dr. Robert Guza
 - Dr. Warren White
- Rutgers University
P.O. Box 231
New Brunswick, NJ 08903-0231
 - Dr. Dale Haidvogel
 - Dr. Kate Hedstrom
- Stevens Institute of Technology
Hoboken, NJ 07030
 - Dr. Lie-Yauw Oey
 - Dr. Yu. Benilov
- University of California
Irvine, CA 92717
 - Dr. Carl Friehe
 - Dept. of Geosciences
- Prof. Geoffrey Vallis Dept. of Marine Sciences
University of California
Santa Cruz, CA 95064

- San Jose State University
Dept. of Meteorology
1 Washington Square San Jose, CA 95192-0104
- Dr. R. L Street
Environmental Fluid Mechanics Laboratory
Stanford University
Stanford, CA 94305-4020
- Mississippi State University
Engineering Research Center
P.O Drawer 6176
Mississippi State, MS 30762
 - Dr. Bharat Soni
 - Dr. Joe Thompson
- Mississippi State University
Center for Air Sea Technology
Building 1103
Stennis Space Center, MS 39529
 - Mr. Jim Corbin
 - Dr. David Dietrich
 - Dr. Lanny Yeske
- University of Southern Mississippi
Building 1103
Stennis Space Center, MS 39529
 - Dr. Grayson Rayborn
 - Dr. Ranjit Passi
 - Dr. Germana Peggion
 - Dr. Louise Perkins
 - Dr. Ziv Sirkes
 - Mr. Robert Willems
 - Center for Marine Science
- Prof. Anderson
The Ocean Climate Research Division
Dept. of Atmospheric & Oceanic Sciences
University of Wisconsin-Madison
1225 West Dayton Street
Madison, WI 53706

- Dr. John Apel
Applied Physics Laboratory
Johns Hopkins University
Laurel, MD 20723
- Prof. Jackson Blanton
Skidaway Institute of Oceanography
Savannah, Georgia 31416
- Dr. Alan Blumberg
Hydro-Qual, Inc.
1 Lethbridge Plaza
Mahway, NJ 07430
- Dr. George Forristal
Shell Development Company
P.O. Box 481
Houston, TX 77001
- Dr. Lee-Lueng Fu
Jet Propulsion Laboratory
California Institute of Technology
4800 Oak Grove Drive
Pasadena, CA 91109-8099
- Dr. Michael Ghill
University of California
Los Angeles, CA 90024
- Dr. Lakshmi Kantha
University of Colorado
Campus Box 431
Boulder, CO 80309-0431
- Dr. A. D. Kirwan
Dept. of Oceanography
Old Dominion University
Norfolk, VA 23529-0276
- Dr. Aaron Lai
Los Alamos National Laboratory
Los Alamos, NM 87545
- Dr. Richard Miksad
Dept. of aerospace Engineering & Engineering Mechanics
The University of Texas at Austin
Austin, TX 78712-1085

- Dr. Stephen Murray
Louisiana State University
Coastal Studies Institute
Baton Rouge, LA 70803-7527
- Markku Santala
Exxon Production Research Co.
P.O. Box 2189
Houston, TX 77252-2189
- Dr. David Szabo
Mobil Research & Development Corp.
Offshore Engineering
13777 Midwam Road
Farmers Branch, TX 75234
- Dr. William O'Connor
NOAA Great Lakes
Environmental Research Laboratory
2205 Commonwealth Blvd
Ann Arbor, MI 48105
- Dr. Dave Peters
Conoco Incorporated
600 N. Ashford
P.O. Box 2197
Houston, TX 77252
- Prof. Eugene Takle
Atmospheric Science
3010 Agronomy Hall, ISU
Ames, IA 50011
- University of Washington
Dept. of Oceanography
Seattle, WA 98195
- Asian Institute of Technology
G. P.O. Box 2754 Bangkok 10501
ThaiLand
- Institute of Oceanographic Sciences
Deacon Laboratory
Brook Road, Wormley
Godalming, Surrey GU8 5UB United Kingdom
- Dr. Ian Jones
Ocean Technology, J05

University of Sydney
NSW 2006 Australia

- Dr. M. Kuzmic
Ruder Boskovic Institute
P.O. Box 1016, 41001 ZAGREB, CROATIA
- Dr. Ruben Morales
School of Ocean Sciences
Unit for Coastal and Estuarine Studies
Menai Bridge, Gwynedd LL59 5EY
United Kingdom
- Dr. Ing Wolfram Schrimpf
Joint Research Center of CEC
Institute for Remote Sensing Applications
Bldg 69 T.P. 690, I-21020 Ispra (VA), ITALY
- Prof. Ann Henderson-Sellers
Climate Impacts Center
School of Earth Sciences
Suite 616, E7A, Macquarie University
New South Wales, 2109 Australia
- Dr. Alex Warn-Varnas
SACLANT Undersea Research Center
Viale san Bartolomeo, 400
19138 san Bartolomeo
La Spezia, Italy

DUDLEY KNOX LIBRARY



3 2768 00329113 9